The Effect of Composition on the High Pressure Behavior of Rare-Earth Phosphate Minerals

Karina M. Heffernan

Thesis submitted to the faculty of the Virginia Polytechnic Institute and State University in partial fulfillment of the requirements for the degree of

Master of Science
In
Geosciences

Prof. Nancy L. Ross
Dr. Carla Slebodnick
Prof. Robert J. Tracy
Prof. Mark J. Caddick
Prof. F. Marc Michel

May 31st 2016
Blacksburg, Virginia

Keywords: Monazite, Xenotime, High-Pressure, Diffraction, Raman

The Effect of Composition on the High Pressure Behavior of Rare-Earth Phosphate Minerals

Karina M. Heffernan

Abstract

A comprehensive study on the effect of composition on the structural and elastic properties of MPO_4 ($M = Ce^{3+}$, Gd^{3+}, Tb^{3+}, Y^{3+}, Sc^{3+}) compounds has been completed. $CePO_4$ and $GdPO_4$ are isostructural with monazite ($P2_1/n$), and $TbPO_4$, YPO_4, and $ScPO_4$, are isostructural with xenotime ($I4_1/amd$). Raman spectra are consistent with previous studies and high-pressure spectra showed no phase transitions up to 10 GPa under hydrostatic conditions. The spectra were used to develop Kieffer-type lattice vibrational models to calculate heat capacities of $CePO_4$ and YPO_4 and the results lie within 1-3% of experimental values. Equations of state were calculated from high-pressure single-crystal X-ray diffraction data. Bulk moduli (K_0) determined from a 3rd-order Birch-Murnaghan equation of state are: 109(3) GPa for $CePO_4$, 128.1(8) GPa for $GdPO_4$, 141(1) GPa for $TbPO_4$ and 166(1) GPa for $ScPO_4$. The inverse relationship observed between K_0 and the ionic radius of the RE^{3+} is shown to be linear. This equation can be used to predict K_0 for other rare-earth phosphates. Comparison of these studies, performed under hydrostatic conditions, with previous studies show that MPO_4 structures are sensitive to shear stresses created from non-hydrostatic environments. The first structural study of a monazite, $GdPO_4$, is also reported. Compression mechanisms are comprised of "squishing" the GdO_9 polyhedra and inter-polyhedral movement. This study and the axial compressibility data for Ce-, Tb-, Gd- and $ScPO_4$ suggest that the compression mechanisms favored by MPO_4 compounds are those which remain rigid parallel to polyhedral chains.

Author Acknowledgements

First and foremost, I would like to thank my committee and in particular my advisor Prof. Nancy Ross. You gave incredibly valuable insight and assistance with all aspects of this project, without your guidance nothing would have been accomplished. I appreciate all you have done for me and I want to thank you for helping me start my professional journey.

I would like to thank the Virginia Tech Crystallography (VTX) group, especially Dr. Elinor Spencer and Dr. Jing Zhou for patiently teaching me numerous laboratory skills and helping me learn to think like a scientist. You both always stopped whatever you were doing to give me a hand when I asked for one and I hope you know how much this is appreciated.

I would also like to thank Dr. Lynn Boatner at Oak Ridge National Lab for providing the synthetic samples used in this thesis. Of course, without Dr. Boatner none of this research would have been possible.

I would like to thank Mr. Charles Farley, and Prof. Robert Bodnar for the use of and their assistance with the Virginia Tech Raman lab. I would also like to thank Prof. Roberty Tracy for his assistance with the Virginia Tech Microprobe Lab.

Lastly I would like to extend a huge thank you to my fellow graduate students, my friends and family, and my tea buddies, for always listening and offering a kind to word. I certainly could not have done this without you.

Grant Information

This research was supported by the National Science Foundation grant EAR-1118691 to Dr. N.L. Ross. The Geological Society of America, and the American Crystallographic Association both provided travel grants to attend their respective conferences.

Table of Contents

Chapter 3: Equation of State of Rare-Earth Phosphates

Chapter 4: The Structural Response of Gadolinium Phosphate to Pressure

Chapter 5: Conclusion

List of Figures

List of Tables

Attribution

Manuscript of Chapter 4:

The Structural Response of Gadolinium Phosphate to Pressure
Karina M. Heffernan, Nancy L. Ross, Elinor C. Spencer, Lynn A. Boatner, *J. Solid St. Chem*., Submitted, **(2016)**

Karina M. Heffernan was responsible for data collection, data analysis, and preparation of the manuscript under the supervision of Dr. Elinor C. Spencer and Prof. Nancy L. Ross.

Lynn A. Boatner was responsible for synthesis of the gadolinium phosphate sample used in data collection.

Chapter 1: Introduction

1.1 Background

The study of mineral properties, such as their thermodynamic behaviors, crystalline structures, phase transformations, etc., is fundamentally important for understanding the relationship between microscopic effects that occur on the atomic scale and broad-scale geologic processes. For example, an appreciation of the elastic behavior of minerals is essential for the modeling of earthquakes,[1] the chemistry and thermodynamics of minerals dictates their distribution throughout the environment,[2] and structural phase transformations are essential to rock formation.[3] The research reported in this thesis focuses on an assessment of the structural and thermodynamic properties of rare-earth phosphate minerals, with the general formula MPO_4 (M = trivalent lanthanide metal).

MPO_4 minerals are of particular relevance as ores for technologically important rare earth elements (REEs)[†].[4] Indeed, much of the world's technological infrastructure depends directly on the these elements as they are incorporated in a vast array of devices such as lasers, electronic screens, permanent magnets, battery alloys, and ceramics. The United States was a major contributor to the global REE market but this changed in the late 1980s when the Mountain Pass mine in California closed. Currently, 97% of the world's supply of these essential metals is provided by China, and due to increasing demand and political pressures there is considerable global interesting in finding and exploiting new deposits and improving extraction processes.[5,6] Yet, if these advancements are to be made, it is critical that the physical and chemical properties of MPO_4 minerals be understood fully.

The three most highly utilized REE ores are the carbonate mineral bastnäsite, $M(CO_3)F$ (M = Ce, La, Y), and the MPO_4 dimorphs monazite and xenotime. Monazite contains the larger, lighter REEs (La, Ce, Pr, Nd, Pm, Sm, Eu, and Gd), whereas xenotime contains the smaller, heavier REEs (e.g. Tb, Dy, Ho, Er, Tm, Yb, Lu, Sc, and Y). These phosphate minerals are considered widespread accessory minerals meaning that they occur in a vast number of geologic environments (both metamorphic and igneous) but rarely make up a more than a small percentage of the overall bulk rock concentration. The most common occurrence of monazite and xenotime are within igneous rocks such as rhyolites, pegmatites, granitoids, etc.[7] They are also

[†] According to the IUPAC definition, metals of the lanthanide series as well as yttrium and scandium are also known as rare earth elements. However, it is still debated in certain scientific communities if yttrium and scandium should be included in this definition due to their lack of 4f orbitals.

found in metapelitic rocks and as detrital grains.[8] They generally form alongside a variety of other igneous minerals, in particular, xenotime frequently crystallizes within garnet crystals. However, due to garnet's incorporation of yttrium, when the overall rock composition is very garnet-rich the presence of xenotime is less common.[8] Figures 1.1a and 1.1b shows two natural specimens of monazite and xenotime in quartz and granite matrices, respectively.

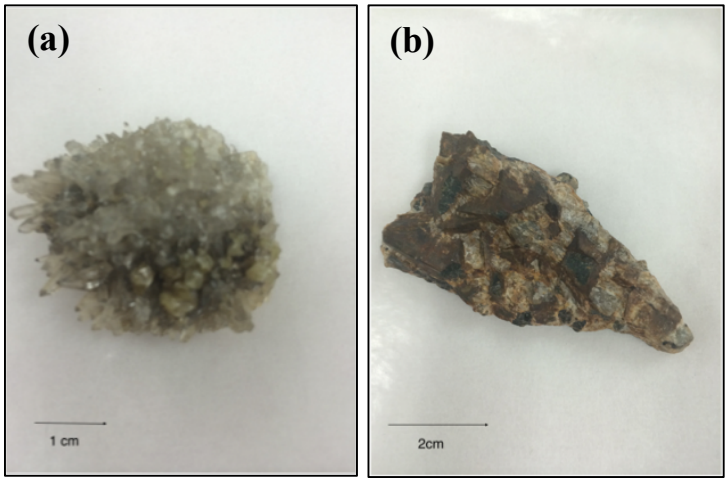

Figure 1.1: Natural Samples of Monazite and Xenotime. (a) A sample of natural monazite embedded in a quartz matrix. The monazite crystals are the greenish crystals near the bottom of the sample. (b) A sample of natural xenotime within a granitic matrix. The xenotime crystals are the block-like dark brown crystals.

Monazite and xenotime are also known for their substitution of thorium (Th) and uranium (U) in the rare-earth cation sites. In monazite, the doping of U and Th can be up to 25%, but is generally less than 5%. In xenotime, concentrations of these actinides are unusually much lower − typically around 1 or 2 %.[8] The incorporation of radioactive elements U and Th, which have half-lives on the order of billions of years, in these minerals gives them an important role as a geochronometers.[9] This method relies on the radioactive decay of U and Tb to Pb for dating geological formations in which they are present.[10] In fact, monazite and xenotime are particularly good geochronometers because they rarely naturally incorporate Pb during their formation, therefore it can be assumed that any Pb present in their structures is radiogenic in origin.[11,12] Furthermore, because they are widespread, they can be used to compare previously uncorrelated geologic environments.

Rare-earth phosphate minerals are also being considered as potential solid-state repositories for nuclear waste.[13] This is because some REEs have high neutron absorption cross-sections (e.g. σ_{abs} = 49700 barns for Gd).[14] Moreover, these compounds do not suffer substantial metamictization, meaning that it requires little energy for them to recrystallize after being

amorphosed.[15] They also are believed to be resilient to pressure (see Chapter 3) and temperature fluctuations. However, as some MPO_4 materials have been shown to be weakly soluble,[16] attention has been focused on their inclusion in more robust ceramic matrices for the construction of spent nuclear fuel canisters.[17]

1.2 Crystal Structures

MPO_4 compounds containing large rare-earth (REE) cations adopt the monazite structure, and crystallize in the monoclinic space group $P2_1/n$. The asymmetric unit comprises a single REE^{3+} ion and one PO_4^{3-} anion (all atoms are located on general positions). The phosphate cation has the expected tetrahedral coordination with no significant distortion. The coordination geometry of the nine-coordinate REE^{3+} ion is best described as a severely distorted mono-capped square antiprism (MCSAP). The packing arrangement of the polyhedra is complex but can be described as chains of alternating PO_4 and $REEO_9$ polyhedra that, in the standard $P2_1/n$ setting, lie parallel to the [100] direction. These chains are then cross-linked via bridging oxygen atoms between the REE^{3+} ions. This packing arrangement results in each REE^{3+} being coordinated to seven PO_4 tetrahedra, five of which are vertex sharing, while the remaining two are edge sharing. Furthermore, each REE^{3+} ion shares common edges with six neighboring REE^{3+} cations (Fig. 1.2).

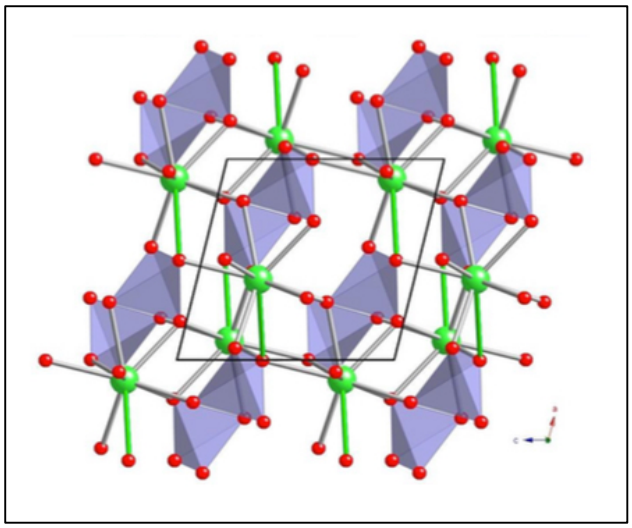

Figure 1.2: Crystal structure of Monazite. Structure viewed down [010]. The green and red spheres represent REE^{3+} ions and oxygen atoms, respectively. The REE-O capping bonds of the MCSAP polyhedra are shown in green. The PO_4 tetrahedra are shown in

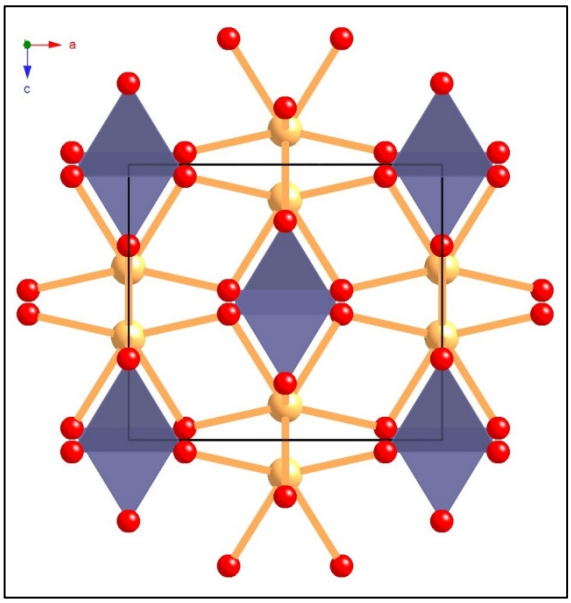

Figure 1.3: Crystal Structure of Xenotime. Structure viewed down [010]. The orange and red spheres represent REE^{3+} ions and oxygen atoms, respectively. The PO_4 tetrahedra are shown in light purple.

Phosphates containing small REEs assume xenotime structures, and crystallize in the tetragonal space group $I4_1/amd$. In this case, all atoms of the asymmetric unit are situated on special positions. The eight-coordinate REE^{3+} ion is located on a position of -4m2 symmetry (Wyckoff position 4*a*), resulting in a highly symmetrical $REEO_8$ polyhedron.[18] The polyhedron is constructed from two edge sharing and four vertex sharing PO_4 tetrahedra. These tetrahedra are regular in shape with -4m2 symmetry (the phosphorous atoms resides on Wyckoff position 4*b*).

As in the case of monazite, the REE^{3+} polyhedra and PO_4 tetrahedra in xenotime alternate to form chains, which in the standard $I4_1/amd$ setting, lie parallel to the [001] direction and are cross-linked by PO_4 tetrahedra (Fig. 1.3).

Although both xenotime and monazite share common structural features, such as cross-linked chains of alternating $REEO_x$ and PO_4 tetrahedra, the critical difference is the coordination environment of the REE^{3+} ions (Fig. 1.4). In monazite the REE^{3+} cations are nine-coordinate and are bound to seven PO_4 tetrahedra, whereas in the xenotime the REE^{3+}cations are eight-coordinate and are bound to six PO_4 tetrahedra. In both dimorphs, two of the PO_4 tetrahedra of the REE^{3+} coordination sphere are edge sharing, and the remaining tetrahedra are vertex sharing.

These coordination differences are related to the ionic radii of the REE^{3+} cations incorporated in the structures. The larger REE^{3+} cations in monazite can accommodate a higher number of phosphate groups than the smaller cations in xenotime due to a reduction in steric

hinderence. Furthermore, the electronic structure of the REE^{3+} cations, and their coordination environments in these two minerals, results in the REE-O bonds in the nine-coordinated REE^{3+} polyhedra in monazite being longer and weaker than those in the eight-coordinated REE^{3+} polyhedra in xenotime.[19,20] This has implications for the compressibility of these $REEO_x$ polyhedra (see chapters 3 and 4).

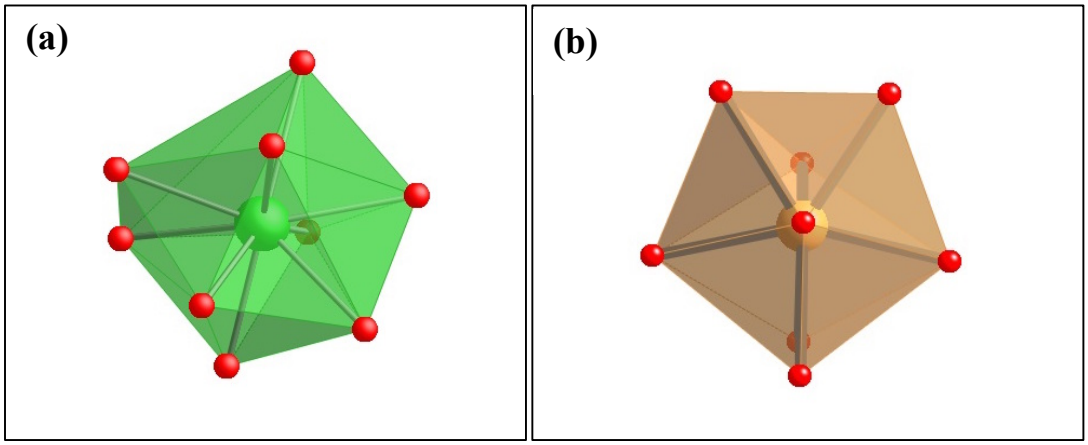

Figure 1.4: Coordination Environments for the REE^{3+} Cations in Monazite and Xenotime Structures. (a) Nine-coordinated REE^{3+} polyhedra in monazite. (b) Eight-coordinated REE^{3+} polyhedra in xenotime.

1.3 The Bastide Diagram

Figure 1.5 shows a Bastide diagram, which provides a visual representation of the relationship between ionic radii and structural phase for a variety of compounds with the general formula ABO_4.[21,22] The diagram relates the ABO_4 phases to the radii of the A and B cations relative to the radius of O^{2-}. In our case, the A cation for both monazite and xenotime is the REEE, and the B cation is phosphorus. The most interesting regions of this plot are the phase boundaries, and the compounds that lie close to them. Several REEE phosphates (REEE = Y, Dy, Tb and Gd) are situated close to the xenotime/monazite boundary. This suggests that conversion between these phases is feasible upon application of an external stimulus that "mimics" the effect of changing cation radii, namely pressure. The rationale behind this concept is that increasing pressure decreases REE–O bond length, and as the A and B cations are regarded as incompressible, it is the O^{2-} anion that reduces in size.[23] This somewhat simplistic idea does not allow for quantitative assessment of pressure-phase relationships (e.g. predicting the pressure at which transitions will occur), but it has proven somewhat successful in explaining

the transition trends observed for these materials. For example, the Bastide diagram suggests that the following transitions are likely to occur, for MPO_4 compounds, with increasing pressure: xenotime → anhydrite (possibly) → monazite → scheelite, and indeed this sequence is consistent with current experimental observations.[24-28]

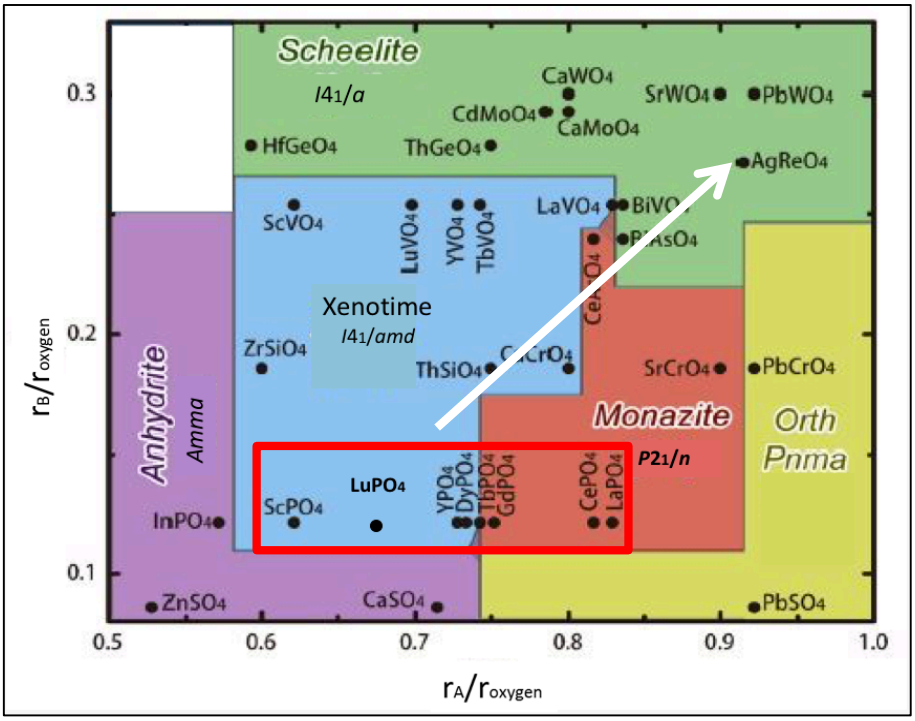

Figure 1.5: A Bastide diagram for ABO_4 compounds. The red box highlights the section of the diagram occupied by phosphates, and the white arrow shows the expected "direction" for pressure-induced phase transitions. Adapted with permission from Yaun, H.; Wang, K.; Wang, C.; Zhou, B.; Yang, K.; Lui, J.; Zou, B. *J. Phys. Chem. C* **2015**, *119*, 8364–8372. Copyright 2015 American Chemical Society.

1.4 This Study

The objective of the research presented in this thesis is to gain a better understanding of the influence of the REE cation on the structural and thermodynamic properties of MPO_4 (M = trivalent lanthanide cation) compounds with monazite and xenotime topologies. In particular, the structural and vibrational behaviors of several monazite and xenotime compounds have been evaluated under pressure, allowing for a systematic assessment of the stability and elastic response of this important class of phosphate materials.

To date, the results from numerous high-pressure studies of xenotime/monazite compounds have been reported in the literature, however although informative, much of it is

conflicting and structure-property correlations cannot be deduced, with any confidence, from the currently available data (reviews of the relevant literature are given in Chapters 2 and 3). To resolve this issue, there is a need for studies that approach the analysis of these compounds in a systematic way. Therefore, the diffraction and spectroscopic measurements presented in this thesis have been conducted under well-defined conditions on xenotime/monazite samples with known compositions, to allow for direct comparison between the result and for reliable determination of any structure-property relationships that are inherent to these materials.

In Chapter 2, a Raman spectroscopy study on a suite of MPO_4 materials is presented. Raman spectroscopy is an important characterization technique that is used to discern the vibrational behavior of both the atomic groups and lattice comprising a material. Raman spectra for the monazite/xenotime samples were collected under both ambient and high pressure conditions. The ambient condition data were used to determine the effect of the REE cation on the vibrational behavior of these mineral structures, and through application of appropriate thermodynamic models, the heat capacity for selected MPO_4 compounds were calculated from these data. The high pressure data were used to determine if any of these materials undergo phase transitions below 10 GPa, and to aid in the elucidation of the compression mechanisms operating in the monazite structure (discussed in Chapter 4).

Chapter 3 details an equation of state (EoS) study performed with four MPO_4 compounds – two with the monazite structure, and two with the xenotime structure. The results from this study highlight the importance of understanding the stress state MPO_4 compounds are subjected to when measuring their elastic constants. Furthermore, because of the EoS analyses discussed in this chapter were conducted under controlled conditions, an inverse relationship between the ionic radii of REE cations and the bulk moduli of these compounds has been identified.

In Chapter 4, a high-pressure (< 7 GPa) single-crystal diffraction analysis of $GdPO_4$ (monazite) is discussed. This study has permitted the compression mechanisms operating in this structure to be evaluated. This is the first high pressure study of any monazite/xenotime structure to explore these mechanisms in detail. The results of this structural study have been linked to the axial compressions for $GdPO_4$ (Chapter 3) and the results from the high-pressure Raman study of this rare-earth phosphate (Chapter 2).

Finally, Chapter 5 summarizes the key conclusions derived from the extensive systematic monazite/xenotimes studies detailed in preceding three chapters.

References

[1] Moczo, P.; Kristek, J.; Vavryčuk, V.; Archuleta, R. J. Halada, L.; *Bull. Seismol. Soc. Am*. **2002**, *92*, 3042−3066.

[2] Hystad, G.; Downs, R. T.; Grew, E. S.; Hazen, R. M. *Earth and Planet. Sci. Lett.* **2015**, *426*, 154−157.

[3] Putnis, A. "*Introduction to Mineral Sciences*". Cambridge University Press (1992)

[4] Chakhmouradian, A. R.; Wall, F. *Elements* **2012**, *8*, 333−340.

[5] Jordens, A.; Cheng, Y.-P.; Waters, K. E. *Mineral. Eng.* **2013**, *41*, 97−114.

[6] Chen, Z.; *J. Rare Earths* **2011**, *29*, 1−6.

[7] Rafiuddin, M.R.; Mueller, E.; Grosvenor, A. P. *J. Phys. Chem.* **2014**, *118*, 18000−18009.

[8] Spear, F.S.; Pyle, J.M.; "*Apatite, monazite, and xenotime in metamorphic rocks*" in: *Phosphates: Geochemical, Geobiological, and Materials Importance*, *Rev. in Mineralogy and Geochemistry*, Hughes, J. M.; Kohn, M.; Rakovan, J. (Eds.), Vol. 48, Mineralogical Society of America & the Geochemical Society, **2002**.

[9] Parrish, R. *Can. J. Earth Sci.* **1990**, *27*, 1431−1450

[10] Wilby, P. R.; Page, A. A.; Zalasiewicz, J. A.; Milodowski, A. E.; Williams, M.; Evans, J. A. *J. Geol. Soc.* **2007**, *164*, 53−56.

[11] Grove, M.; Harrison, T.M. *Geology*. **1999**, *27*, 487−490.

[12] Parrish, R. R. *Can. J. Earth Sci.* **1990**, *27*, 1431−1450.

[13] Ewing, R. C. *Can. Min.* **2001**, *39*, 697−715.

[14] Sears, V. F. *Neutron News* **1992**, *3*, 29–37.

[15] Nasdala, L.; Irmer, G.; Jonckheere, R. *Contrib. Min. Petrol.* **2002**, *143*, 758–765.

[16] Firsching, F. H.; Brune, S. N. *J. Chem. Eng. Data* **1991**, *36*, 93–95.

[17] Lessing, P.A.; Erickson, A. W. *J. Eur. Ceramic Soc*. **2003**, *23*, 3049–3057.

[18] Ni, Y.; Hughes, J. M.; Mariano, A. N. *Am. Min.* **1995**, *80*, 21–26.

[19] Du, A.; Wan, C.; Qu, Z.; Pan, W. *J. Am. Ceram. Soc.* **2009**, *92*, 2686–2692.

[20] Feng, J.; Xiao, B.; Zhou, R.; Pan, W. *Acta Mater.* **2013**, *61*, 7364–7383.

[21] Bastide, J. P. *J. Solid State Chem.* **1987**, *71*, 115–120.

[22] Yaun, H.; Wang, K.; Wang, C.; Zhou, B.; Yang, K.; Lui, J.; Zou, B. *J. Phys. Chem. C* **2015**, *119*, 8364–8372.

[23] Bondi, A. *J. Phys. Chem.* **1964**, *68*, 441–452.

[24] Lacomba-Perales, R.; Errandonea, D.; Meng, Y.; Bettinelli, M. *Phys. Rev. B.* **2010**, *81*, 064113.

[25] Zhang, F. X.; Wang, J. W.; Lang, M.; Zhang, J. M.; Ewing, R. C.; Boatner, L. A. *Phys. Rev. B.* **2009**, *81,* 184114.

[26] López-Solano, J.; Rodriguez-Hernandez, P.; Munoz, A.; Gomis, O.; Santamaria-Perez, D.; Errandonea, D.; Manjon, F. J.; Kumar, R. S. Stavrou, E.; Raptis, C. *Phys. Rev. B.* **2010**, *81,* 144126.

[27] Zhang, F. X., Lang, M.; Ewing, R. C.; Lian, J.; Wang, Z. W.; Hu, J.; Boatner, L. A. *J. Sol. State Chem.* **2008**, *181*, 2633–2638.

[28] Tatsi, A.; Stavrou, E.; Boulmetis, Y. C.; Kontos, A. G.; Raptis, Y. S.; Raptis, C. *J.Phys.: Cond. Matter.* **2008**, *20*, 425216.

Chapter 2: Raman Spectroscopy of Rare-Earth Phosphates

2.1 Introduction

Raman spectroscopy is an important characterization technique that is used to discern the atomic groups within a material by observing the material's interaction with light. The strength of these interactions is based upon bonding characteristics, as well as the configuration and symmetry of the atomic groups. These properties produce Raman active modes that are used to fingerprint different functional groups.[1]

The interatomic vibrational information given by Raman spectroscopy makes it an important and useful technique that is complementary to X-Ray diffraction. Since Raman spectroscopy is a non-destructive technique it is commonly used in conjunction with other analyses. Furthermore, the atomic vibrations observed though Raman spectroscopy contribute considerably to a material's thermodynamic properties.[2-6] This relationship is something that will be discussed in more detail later on in this chapter.

2.1.1 Factor Group Analysis and Mode Assignments

The factor group analysis for rare-earth phosphate minerals monazite and xenotime have been previously reported in studies by Begun et al.[7], Silva et. al.[8] and Giarola et. al.,[9] respectively. Factor group analysis is an empirical method that assigns symmetry features to vibrational modes based on known crystallographic properties.[10] The total number of vibrational modes of a crystalline solid is 3N where N is the number of atoms in the primitive unit cell. Of these modes, 3 are acoustic (translational) modes that can be measured by methods such as Brillouin spectroscopy,[11] and 3N-3 are optical modes that can interact with photons. Raman spectroscopy and infrared spectroscopy are commonly used to characterize the optical modes of crystalline materials. Crystals with lower symmetry tend to have more atoms in the primitive unit cell, and therefore a higher number of expected optical modes.[12]

Monazite (space group $P2_1/n$) has 24 atoms in its primitive unit cell and therefore 69 optical modes. Of these 69 modes, 36 are predicted to be Raman active and 33 are predicted to be infrared active.[7] The Raman modes have assignments of A_g or B_g which are singly degenerate symmetric lattice modes. Factor group analysis predicts there are 18 A_g modes and 18 B_g modes.

Table 2.1 shows mode assignments for monazite from Silva et. al.[8] based on their results from polarized Raman, infrared reflectance, and neutron inelastic scattering measurements. Four of the modes are related to the interactions within the PO_4 tetrahedra, two bending (v_2, and v_4) and two stretching (v_1 and v_3). The remainder are complex lattice modes that involve interaction between the GdO_9 polyhedra and PO_4 tetrahedra. Similar to the earlier study of Begun et al.[7], Silva et al[8] observe only 22 peaks in the Raman spectrum of $GdPO_4$, while 18 Ag /18 Bg vibrations are predicted by group theoretical analysis. Additional peaks are observed above 450 cm^{-1} (547, 580, 607, 1003, 1039 and 1091 cm^{-1}). Silva et al.[8] concluded that these peaks arise from infrared transitions activated by defects inducing lowering of a local symmetry so that they appear in the Raman spectra.

Table 2.1 $GdPO_4$ (monazite) Raman Mode Assignments from Silva et. al.[8]

Peak (cm^{-1})	***Symmetry***	***Assignment***
87	B_g	Lattice
108	A_g	Lattice
158	A_g	Lattice
162	B_g	Lattice
178	B_g	Lattice
192	A_g	Lattice
236	A_g/B_g	Lattice
247	A_g/B_g	Lattice
268	A_g	Lattice
302	A_g	Lattice
406	A_g/B_g	Lattice
428	A_g/B_g	Lattice
478	A_g/B_g (v_2)	PO_4 symmetric bend
634	A_g/B_g (v_4)	PO_4 asymmetric bend
988	A_g/B_g (v_1)	PO_4 symmetric stretch
1072	A_g/B_g (v_3)	PO_4 asymmetric stretch

Xenotime ($I4_1/amd$) has 12 atoms in its primitive unit cell and therefore a total of 33 optical modes. Of these 33 modes, only 12 peaks are predicted to occur in the Raman spectrum.[7] Table 2.2 and 2.3 show Giarola et.al.'s[9] mode assignments for $ScPO_4$ and YPO_4 xenotime, respectively, as determined from polarized Raman spectroscopy and first-principles calculations. Seven of the Raman modes, (2A1g + 2B1g + 1B2g + 2Eg), are usually referred to as internal modes as they originate from the internal vibrations of oxygen atoms in the PO_4 tetrahedra. Three of these modes are related to the interactions within the PO_4 tetrahedra, one bending (v_2) and two P-O stretching modes (v_1 and v_3). Four modes (2B1g + 2Eg) are referred to as external modes due to translations of the PO_4 and REE^{3+} ions. One mode (Eg) is the librational mode of the whole PO_4 tetrahedra. The results of the vibrational studies for monazite[8] and xenotime[9] were used to assign all modes from Raman spectra collected in this study.

Table 2.2 $ScPO_4$ (xenotime) Experimental Raman Mode Assignment from Giarola et. al.[9]

Peak (cm^{-1})	***Symmetry***	***Assignment***
187	E_g (1)	Lattice
234	E_g (2)	Lattice
245	B_{1g} (1)	Lattice
326	B_{2g} (v_2)	PO_4 symmetric bend
336	E_g (3)	Lattice
350	B_{1g} (2)	Lattice
474	A_{1g} (1)	Lattice
595	E_g (4)	Lattice
677	B_{1g} (3)	Lattice
1027	A_{1g} (2) (v_1)	PO_4 symmetric stretch
1044	E_g (5)	Lattice
1083	B_{1g} (4) (v_3)	PO_4 asymmetric stretch

Table 2.3 YPO_4 (Xenotime) Experimental Raman Mode Assignment from Giarola et. al.[9]

Peak (cm^{-1})	*Symmetry*	*Assignment*
155	E_g (1)	Lattice
185	B_{1g} (1)	Lattice
209	E_g (2)	Lattice
299	E_g (3) (v_2)	PO_4 symmetric bend
316	B_{1g} (2)	Lattice
331	B_{2g}	Lattice
485	A_{1g} (1)	Lattice
581	E_g (4)	Lattice
659	B_{1g} (3)	Lattice
1001	A_{1g} (2) (v_1)	PO_4 symmetric stretch
1026	E_g (5)	Lattice
1058	B_{1g} (4) (v_3)	PO_4 asymmetric stretch

This chapter presents results of a systematic Raman spectroscopy study on a suite of rare-earth phosphate minerals measured under ambient conditions and at high pressure. The spectra collected under ambient conditions are presented first, as well as the mode assignments for these spectra based on the factor group analyses discussed in section 2.1.1. Collecting spectra on all samples under the same conditions allowed for a better understanding of the effect of the different rare-earth cations on the structure dynamics across the mineral groups. The high-pressure Raman spectra are then presented. These studies served as a precursor to the high-pressure X-ray diffraction experiments to determine whether any phase transitions occur between 1 bar and 9 GPa. The last portion of this chapter uses the input from the spectroscopic data as the basis of constructing lattice vibrational models using the Kieffer model[2-6] and reports the calculation of heat capacities of both monazite and xenotime based on these models.

2.2 Experimental Methods

2.2.1 Raman Spectroscopy under Ambient Conditions

Raman spectra were collected on the rare-earth phosphate minerals $CePO_4$, $GdPO_4$, YPO_4, and $ScPO_4$. The $GdPO_4$, YPO_4, and $ScPO_4$ samples were synthesized via a high-temperature solution growth method by Lynn Boatner at Oak Ridge National Laboratory (TN,

USA).[13] The $CePO_4$ sample was kindly provided by Robert Tracy from a mine located in Hiddenite, North Carolina (USA). An electron microprobe analysis of this sample yielded $Ce_{0.44}La_{0.21}Nd_{0.18}Pr_{0.06}Gd_{0.04}Th_{0.03}Sm_{0.02}Ca_{0.01}Y_{0.01}(P_{0.98}Si_{0.02}O_4)$. However, for convenience this sample will be denoted as $CePO_4$ in this thesis. This composition was determined on a Cameca SX-50 Electron Probe Microanalyzer in which P, Si, Th, Y, La, Ce, Pr, Nd, Gd, U, Ca, and Sm were analyzed. The crystal was mounted, polished, and loaded into the probe which was operating at a voltage of 20kV and 25nA. The sample was analyzed for 50 runs over 500μm, which took about 3.5 h.

The Raman spectra were collected from unoriented single crystals mounted on a glass slide. Spectra were recorded on a JY Horiba LabRam HR spectrometer fit with a 40x objective and equipped with a red laser ($\lambda = 632.817$ nm). The spectral slits were 150 μm in size, and the confocal hole was set to 400 μm. The spectrograph grating had 600 grooves/mm and there was a data collection time of 5 seconds per crystal.

2.2.2 High-pressure Raman spectroscopy

Synthetic $GdPO_4$, and $ScPO_4$ crystals were loaded into a Brillouin-Raman (BR-series) DAC (High-Pressure Diamond Optics, Inc., U.S.A) fitted with two type-IIa diamonds, both 600 μm in diameter. These diamonds, along with others in their class, have very low levels of impurities and, therefore, display negligible photoluminescence. The sample chamber (~300 μm in diameter) was drilled in a steel gasket that was fitted between the diamonds of the DAC. A ruby crystal was also loaded into the DAC for pressure calibration measurements.[14] A 4:1 MeOH:EtOH mixture was added to the chamber to act as the pressure medium, hydrostatic up to 9.8 GPa.[15] High-pressure Raman spectra were recorded on a JY Horiba LabRam HR spectrometer fitted with a 40x objective and equipped with a red laser ($\lambda = 632.817$ nm). The spectral slits were 150 μm in size, and the confocal hole was set to 400 μm. The spectrograph grating had 1200 grooves/mm. Each data collection comprised two scans, each 40 s in duration. The photoluminescence signals (at ca. 694 nm) of the ruby were measured under the same experimental conditions as the sample data collections - except that the scans lengths were varied to adjust the signal intensity when required.

2.3 Results and Discussion

2.3.1 Ambient Raman Spectra

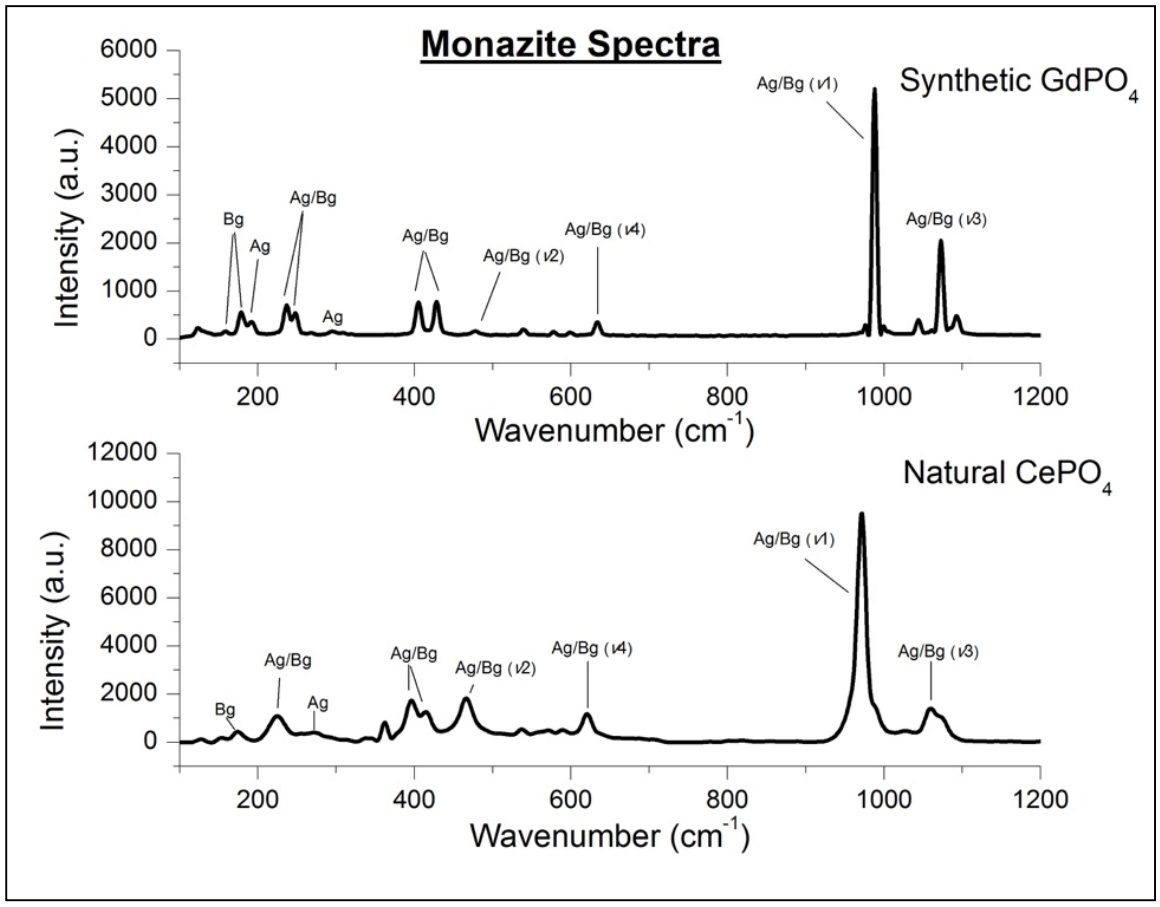

Figure 2.1: Ambient Pressure Monazite Spectra. Raman spectra of $GdPO_4$ and $CePO_4$ monazite single crystals. Spectra span from 100-1200cm^{-1}.

Figure 2.1 shows the ambient pressure Raman spectra of the two monazites, the synthetic $GdPO_4$ and the natural $CePO_4$ sample. The peaks observed in the $GdPO_4$ spectrum show excellent agreement with those reported by Silva et al.[8] However, peaks at 87 and 106 cm^{-1} (Table 2.1) were below the detection level of the Raman spectrometer used in this study and the peak at 158 cm^{-1} was too weak to be resolved. The remaining modes identified in the Raman spectra of Fig. 2.1 are based on the peak assignments from Silva et al.[8] Peaks below 450 cm^{-1} are associated with the lattice modes of the crystal structure and the low-frequency stretching

vibrations of the Gd−O bonds (300−350 cm^{-1}). The v_1, v_2, v_3 and v_4 peaks are associated with internal modes of the PO_4 tetrahedra, where v_2 and v_4 are P-O bending modes and higher frequency v_1 and v_3 are P-O stretching modes. Similar to Silva et al.'s[8] study, additional peaks in the $GdPO_4$ spectrum are observed at 550, 580, 610, 1040 and 1090 cm^{-1} which may be due to infrared transitions activated by defects in the structure.

Overall the $CePO_4$ spectrum shows similarities to the $GdPO_4$ spectrum and peak assignments can be made on the basis of the study of synthetic monazites.[8] The most intense peak present in both spectra is the peak at ca. 990 cm-1 which is assigned to the ν1(PO_4) stretching mode. However, this peak and the others observed are much broader (commonly expressed as FWHMs (full width half maximum)) than those observed for synthetic $GdPO_4$. In addition there are some variations in their Raman shifts (typically toward lower wavenumbers), intensity losses, and the increasing development of asymmetries in the band profiles. There are different causes for peak broadening. Ruschel et al.[16] attributed the broadening to radiation damage in the crystal caused by presence of U (and Th) in the crystals. They found that the Raman-band broadening of natural Ce-bearing monazite can be predicted by the empirical formula relating the full width at half maximum of the main symmetric ν1(PO_4) stretching mode and the sum of the elements (Th + U + Ca + Pb). However, the natural sample of Ce-monazite in this study has low Th content and significant amounts of La Nd incorporated in the structure. Therefore, is most likely that the peak broadening is caused by the extensive incorporation of these elements in the host structure.

Figure 2.2 shows Raman spectra measured under ambient condition for synthetic xenotime samples of $ScPO_4$ and YPO_4. The peaks observed for YPO_4 show excellent agreement with those reported by Giarola et al[8] with 11 of the 12 peaks being observed. The B_{2g} peak at 331 cm^{-1} may have been too weak to be observed. For $ScPO_4$, only 7 of the 12 peaks are observed. The $E_g(2)$ mode that is weak in YPO_4 is not observed in the $ScPO_4$ spectrum. There is a suggestion of a very weak mode corresponding to the $E_g(4)$ mode at 595 cm^{-1}, but the $B_{1g}(3)$ mode is not observed. The absences in the $ScPO_4$ spectra are most likely an effect of orientation as single crystals were used and only one face was examined. In comparison of the Raman spectra of YPO_4 with $ScPO_4$, most of the vibrational modes, either internal or external, show an increase in frequency with the noticeable exception of the $v2$-derived $A1_g(1)$ mode which decreases from ~490 to 480 cm^{-1}, respectively.

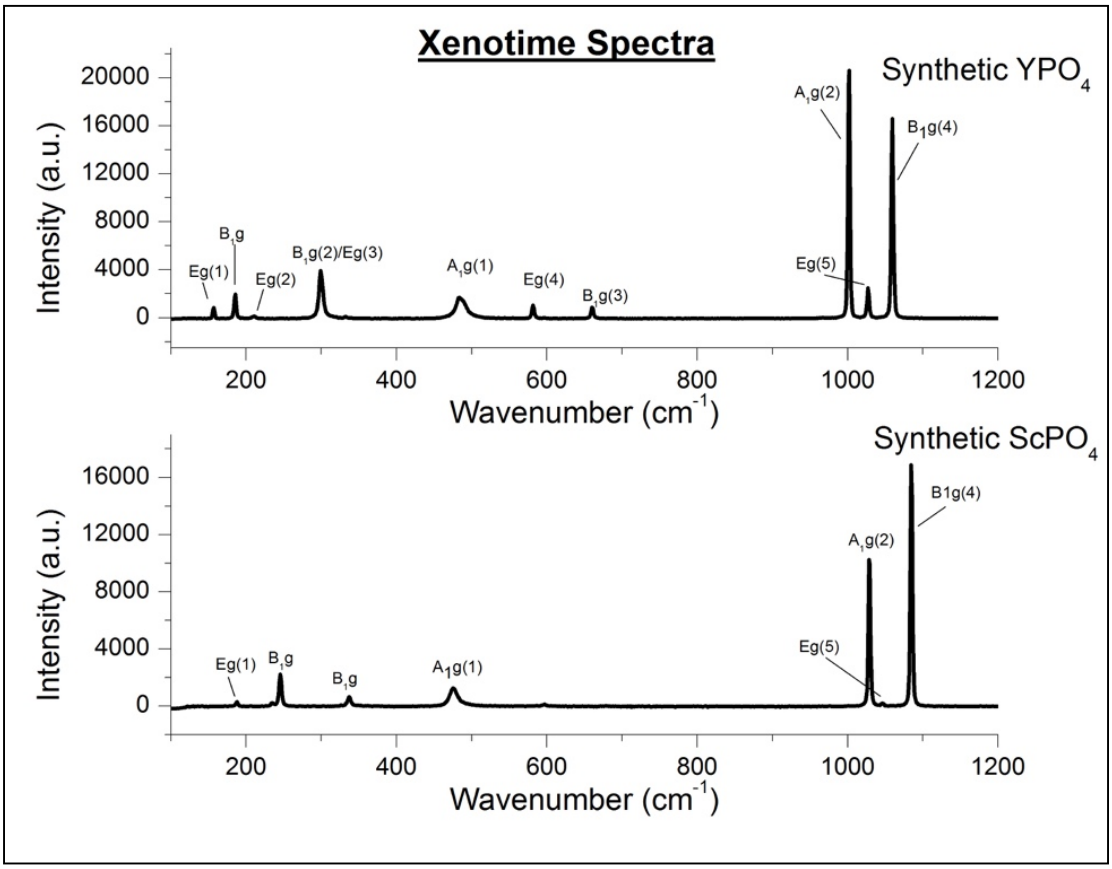

Figure 2.2: Ambient Pressure Xenotime Spectra. Raman spectra of YPO_4 and $ScPO_4$ single crystals. Spectra span from 100-1200 cm^{-1}.

Comparison of the monazite and xenotime Raman spectra shows that monazite has significantly more peaks than the xenotime spectra as xenotime has a higher symmetry than monazite and therefore has fewer atoms in its primitive unit cell. In both, the most intense peaks correspond to the internal PO_4 tetrahedral A_{1g} (ν_1) symmetric stretching modes and B_{1g} (ν_3) asymmetric stretching modes. However, there is a slight increase in wavenumber of these modes from monazite to xenotime. In both, the PO_4 stretching modes are separated from the rest of the modes.

2.3.2 High Pressure Raman Spectra

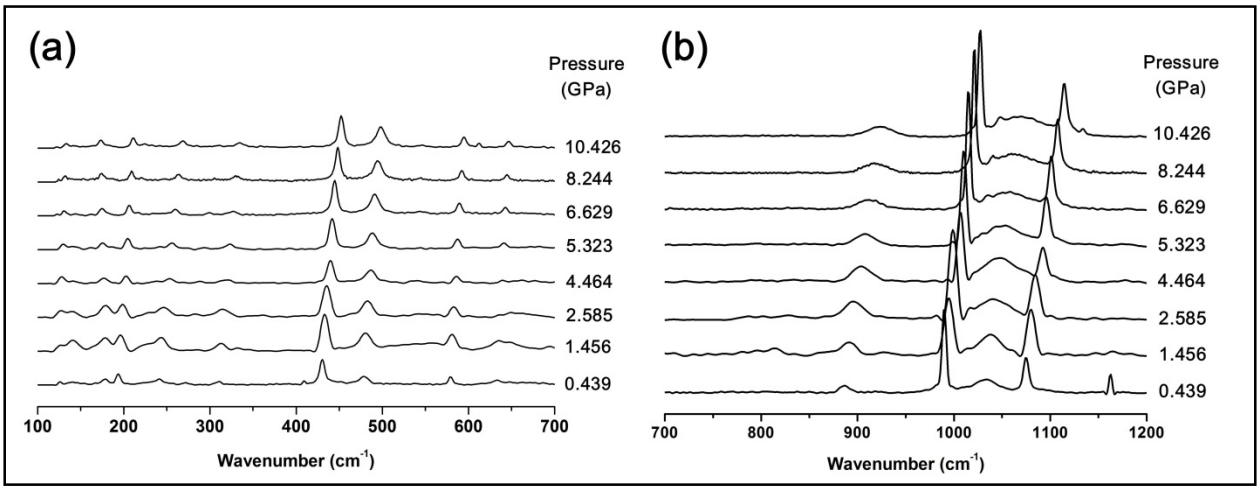

Figure 2.3: High-Pressure Raman Spectra of $GdPO_4$. Variable-pressure Raman data for $GdPO_4$: (a) 100−700 cm^{-1} range; (b) 700−1200 cm^{-1} range. The peak at ~1160 cm^{-1} in the spectrum recorded at 0.439 GPa is an electronic spike and is not sample related. These spectra have been smoothed with a Savitzky−Golay function to enable spectral features to be seen clearly.

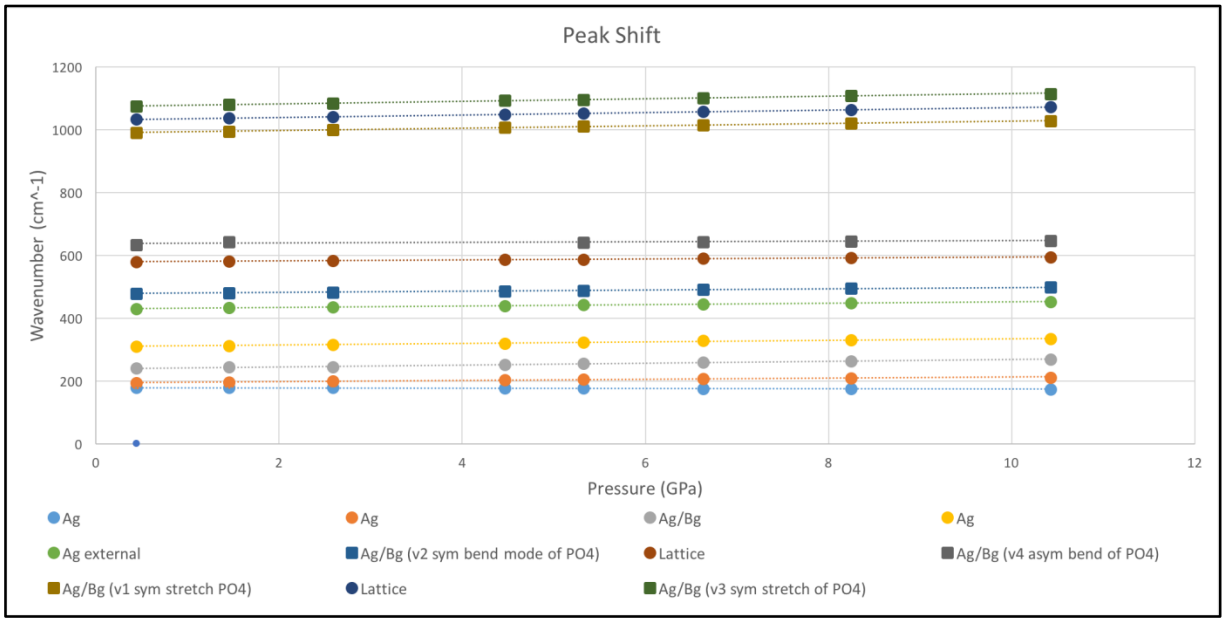

Figure 2.4: Peak Shifts in High-Pressure $GdPO_4$ Spectra. The peak shifts for all assigned modes are shown over the investigated pressure range. Circles represent lattice modes; squares represent PO_4 tetrahedral modes.

High pressure Raman spectroscopy experiments were performed before high-pressure X-ray diffraction experiments (described in Chapters 3 and 4) to determine whether there were any structural transitions over the pressure range studied. Figure 2.3 shows spectra for a high pressure Raman spectroscopy experiment of $GdPO_4$ and Figure 2.4 shows the shifts in peak position for all major modes in the $GdPO_4$ spectra over the investigated pressure range (0−10.426 GPa). There is no evidence of any structural phase transition up to 10.426 GPa. Within the hydrostatic limits of the pressure-transmitting medium ($P < 9.8$ GPa), the spectra are similar. However at 10.426 GPa, additional peaks appear adjacent to the v_3 peak (~1080 cm^{-1}) and between the v_2 and v_4 peaks (580−640 cm^{-1}). This could suggest that the presence of shear stresses further distorts the PO_4 units.

Although no phase transitions are observed at high pressure, there are changes in intensity of the peaks. For example, the v_4 peak (~650 wavenumbers) becomes more pronounced with increasing pressure. This indicates that the pressure-induced distortions that occur within $GdPO_4$ impacts the asymmetric bending of the PO_4 tetrahedra. It is apparent from Figures 2.3 and 2.4 that the bulk of the lattice modes between 100 and 650 cm^{-1} show very little change with pressure. The modes that show the largest shift with pressure are those between 1000 and 1100 cm^{-1} that are associated with the internal stretching modes of the PO_4 tetrahedra. In particular, the v_3 asymmetric stretching mode of the PO_4 tetrahedra shows the greatest shift, $\Delta(v_3)$, of 32.7(1) cm^{-1} between 0.439 and 8.244 GPa yielding a dv/dP of 3.96 cm^{-1}/GPa. This value is similar to that observed for Si-O stretching modes of the SiO_4 tetrahedra in silicates such as forsterite,[17] Mg_2SiO_4 which has a structure in which SiO_4 tetrahedra share oxygen atoms with MgO_6 octahedra. However, in forsterite, the modes that display the greatest shift with pressure are associated with the MgO_6 octahedra and the lowest with the SiO_4 internal modes. This is true for many other silicates where the SiO_4 tetrahedra behave as rigid units under pressure. The high-pressure spectra of monazite therefore suggest that PO_4 tetrahedra may not behave as rigid units under pressure and that the Gd^{3+} cation environment shows little change under pressure. This is investigated further in Chapter 3 where results from a high-pressure crystallographic study of $GdPO_4$ are presented.

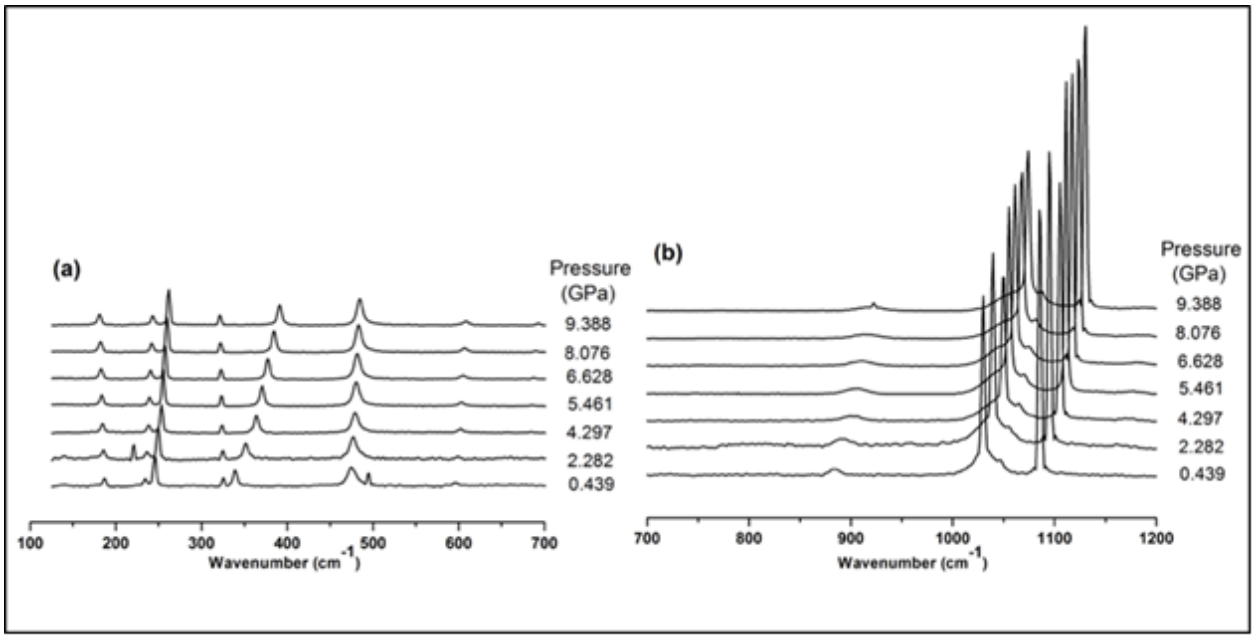

Figure 2.5 High-Pressure Spectra for $ScPO_4$. Variable-pressure Raman data for $ScPO_4$: (a) 100−700 cm^{-1} range; (b) 700−1200 cm^{-1} range. The peak at ~500 cm^{-1} in the spectrum recorded at 0.439 GPa is an electronic spike and is not sample related. These spectra have been smoothed with a Savitzky−Golay function to enable spectral features to be seen clearly.

Figure 2.5 shows high pressure Raman spectra of $ScPO_4$ xenotime between 0.439 and 9.388 GPa and Figure 2.6 shows shifts in assigned peaks over this pressure range. Similar to monazite, these spectra do not show any indication of a phase transition up to 9.388 GPa. The main peak shifts occur in modes ν_1 and ν_3 of the PO_4 tetrahedra at 1020 cm^{-1} and 1070 cm^{-1} respectively that show changes of dv/dP of ~4 cm^{-1}/GPa. These are similar to $\Delta(\nu_3)$ observed in $GdPO_4$ monazite. In contrast to $GdPO_4$, the lattice modes show some variation with pressure. Most notably the B_{1g} mode at 340 cm^{-1} shows a change of dv/dP of 6.4 cm^{-1}/GPa. Interestingly, the Eg mode at 180 cm^{-1} shows a slight *decrease* with pressure which may be associated with distortions in the ScO_8 polyhedra where some atomic group interactions may be moving away from each other with pressure instead of closer together. This may ultimately lead to a structural phase transition. It should be noted that even though more shifts in the vibrational modes are observed in xenotime compared to monazite, the shifts are still small and there are no indications of new (or disappearing modes) or any changes to peak width. Therefore, the changes to the structure are very small and no phase transition or significant structural changes have occurred.

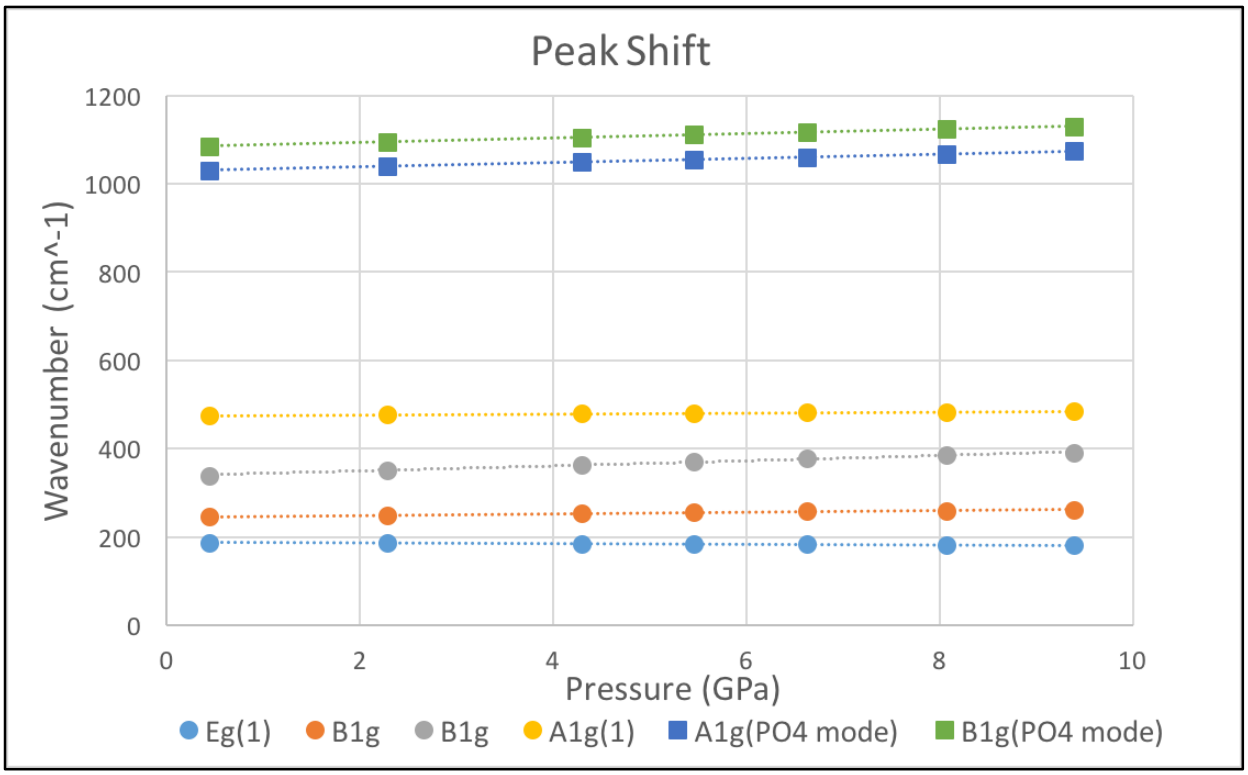

Figure 2.6: Peak Shifts in High-Pressure $ScPO_4$ Spectra. The peak shifts for all assigned modes are shown over the investigated pressure range. Circles represent lattice modes; squares represent PO_4 tetrahedral modes.

2.3.3 Using Spectroscopic Data to Calculate Heat Capacity:

To complement the spectroscopic studies of monazite and xenotime, the heat capacity (C_v) of a $CePO_4$ (monazite) and an YPO_4 (xenotime) were calculated using the Kieffer model[2-6]. The Kieffer model approximates a crystal's vibrational density of states, G(ω), from which its thermodynamic properties can be calculated.[2] The 3 acoustic modes are approximated with sound wave velocity data and the remaining 3N-3 optic modes are approximated from spectroscopic data given above. The calculated heat capacities for both $CePO_4$ and YPO_4 are compared with experimental data.

According to the Kieffer model, the molar isochoric heat capacity normalized to the monoatomic equivalent (C_v^*) is given by the following expression:

$$C_v^* = \frac{N_A k}{nZ}\sum_{i=1}^{3}\varsigma(x_i) + 3N_A k\cdot\left(1-\frac{3}{3nZ}-q\right)\cdot\kappa\begin{pmatrix}x_u\\x_l\end{pmatrix} + 3N_A kq\cdot\varepsilon(x_E) \qquad \textbf{Equation 2.1}$$

where $N_A = 6.023 \times 10^{23}$ mol^{-1}, $k = 1.380 \times 10^{-16}$ ergs deg^{-1}, n = number of atoms in the formula unit, Z = number of formula units in the Bravais unit cell, x_i = dimensionless frequency of acoustic mode i, $\varsigma(x_i)$ = dispersed acoustic function, q = proportion of vibrational modes assigned to the Einstein oscillator, $\kappa\begin{pmatrix} x_u \\ x_l \end{pmatrix}$ = optic continuum function, x_u = dimensionless frequency of the upper limit of the optic continuum, x_l = dimensionless frequency of lower limit of the optic continuum, $\varepsilon(x_E)$ = Einstein function. The values for the dimensionless frequencies can be calculated from a given wavenumber (w) or angular frequency (ω) by use of the equations $x = 2\pi c\hbar w/kT = \hbar\omega/kT$, where $c = 3 \times 10^{10}$ cm s^{-1}, $\hbar = 1.0544 \times 10^{-27}$ ergs s, and T = temperature (K). Values for the dispersed acoustic, optic continuum, and Einstein functions can be taken from the tabulated values reported by Kieffer[4] (as done in this case) or calculated directly with the mathematical functions detailed within that article. The angular frequencies (ω_i) of the acoustic modes can be calculated from values of the spatially averaged acoustic velocities (u_i given in km s^{-1}) with the expression $\omega_i = u_i \cdot K_{max} \cdot (2/\pi)$, where $K_{max} = (6\pi^2/V)^{-1/3}$ and V = volume of unit cell volume (km^3); K_{max} is the radius of a sphere with the same volume as the first Brillouin zone.

To complete these calculations all of the necessary input data must first be calculated. The acoustic modes are calculated from sound velocity data and the spectroscopic data is used to determine the optic continuum and Einstein oscillators. As mentioned above, all of the calculations are based on the fundamental vibrating unit of the crystal which is defined as the number of atoms in the primitive unit cell. For these samples monazite crystallizes in space group $P2_1/n$ and therefore is already in a primitive cell, no transformations are needed. Xenotime however, crystallizes in space group $I4_1/amd$ and must be transformed from a body centered cell to a primitive cell.

Table 2.4 shows the input parameters used for the acoustic modes for both $CePO_4$ monazite and YPO_4 xenotime. Here, the longitudinal velocity (Vp) is calculated from density, bulk modulus, and shear modulus ($Vp = \sqrt{(\frac{K+\frac{4}{3}\mu}{\rho})}$). The shear velocity (Vs) is calculated from shear modulus and density ($Vs = \sqrt{(\frac{\mu}{\rho})}$). The shear modulus and bulk modulus values were taken from Mogilevsky et. al.,[18] and Lacomba-Perales et.al.[19] for YPO_4 and from Feng et. al.[20] for

$CePO_4$. The bulk modulus of $CePO_4$ was determined as part of this dissertation as described in Chapter 3.

Table 2.4 Acoustic Input Parameters for YPO_4 (xenotime) and $CePO_4$ (monazite)

Mineral	*Volume Unit Cell (Angstroms^3)*	*Density (g/cm^3)*	*Bulk Modulus (GPa)*	*Shear Modulus (GPa)*	*Longitudinal Velocity (km/s)*	*Shear Velocity (km/s)*
YPO_4	143.13	4.27	149	56	6.82	3.62
$CePO_4$	301.79	5.26	109	58	5.26	3.38

Table 2.5 Optic Continuum and Einstein Oscillator Input Parameters for YPO_4 (xenotime) and $CePO_4$ (monazite)

Mineral	*Z*	*n*	*q*	*E1 (cm^{-1})*	*E2(cm^{-1})*	*ωl(cm^{-1})*	*ωu(cm^{-1})*
YPO_4	2	6	0.22	1000	1060	165	670
$CePO_4$	4	6	0.11	970	1065	113	615

The spectroscopic data shown in Figures 2.1 and 2.2 were used to approximate the distribution of the optic modes for the Kieffer models. It is noteworthy that in both monazite and xenotime, there is continuous range of lattice modes from 113 cm^{-1} to 615 cm^{-1}, and 165 cm^{-1} to 670 cm^{-1}, respectively. There are no modes observed between these lattice modes and the PO_4 stretching modes that occur around 1000-1100 cm^{-1}. To be consistent with the data, Kieffer models were developed consisting of a single optic continuum and two Einstein oscillators to model v_1 and v_3 of the PO_4 tetrahedra. Table 2.5 summarized the input parameters for both the optic continuum and Einstein oscillators. Here, Z is the number of molecules in the primitive unit cell, n is the number of atoms per formula unit, ω_l and ω_u represent the cutoffs of the optic continuum and q is the proportion of modes assigned to the Einstein oscillators. The model developed by Kieffer for zircon,[6] which is isostructural with xenotime, was used for guidance in assigning *q*.

From these input parameters the isochoric heat capacities were calculated using equation 2.1. Figures 2.7 and 2.8 show all of the individual contributions from the acoustic, optic, and Einstein modes to the overall heat capacity for YPO_4 and $CePO_4$, respectively. In both monazite and xenotime, the figures show that almost the entire contribution to the heat capacity comes

from the acoustic modes below 100 K. However, above 300 K the main contribution is from the optic and, to a lesser extent, the Einstein oscillators.

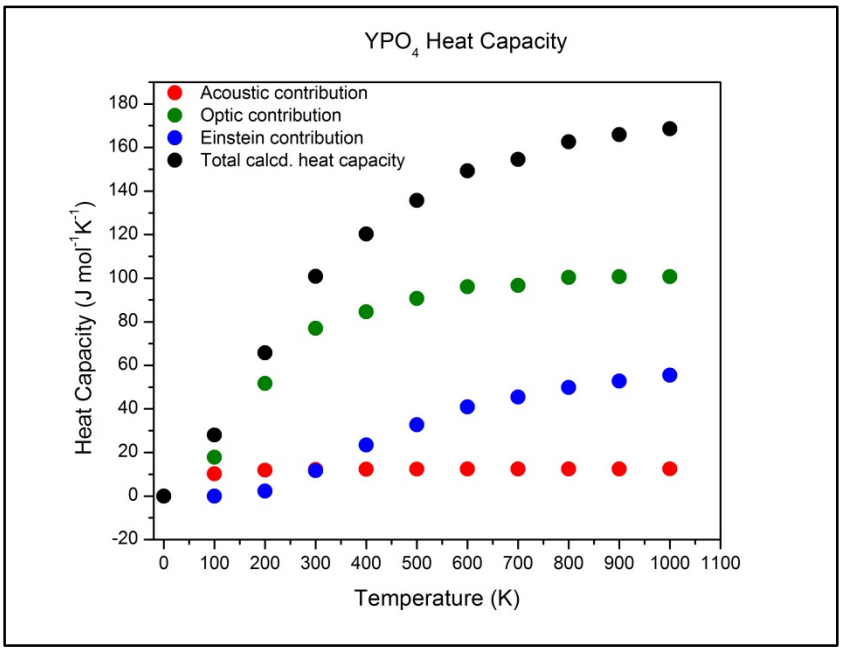

Figure 2.7: YPO_4 Heat Capacity Contributions. Total calculated heat capacity is shown in black, acoustic contribution is in red, Einstein contribution is shown in blue, and optic contribution is shown in green.

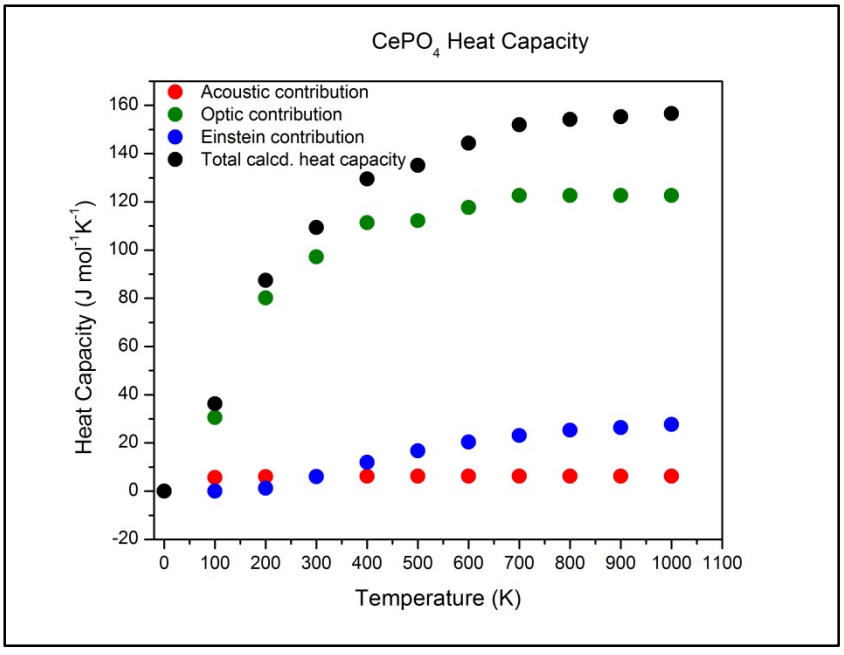

Figure 2.8: $CePO_4$ Heat Capacity Contributions. Total calculated heat capacity is shown in black, acoustic contribution is in red, Einstein contribution is shown in blue, and optic contribution is shown in green.

Tables 2.6 and 2.7 show the values of the calculated heat capacities for YPO_4 and $CePO_4$, respectively, from 0 to 1000 K. For YPO_4, C_v of 100.8 J/mol-K at 300 K was calculated and for $CePO_4$ a value of 109.4 J/mol-K at 300 K was calculated. To compare with experiments the isochoric molar heat capacity, C_v, should be converted to the isobaric molar heat capacity, C_p. C_p is related to C_v by the expression $C_p = TV_m \alpha^2/\beta + C_v$ where V_m is the molar volume, α is the volumetric coefficient of thermal expansion, and β is the isothermal compressibility. Typical values for the conversion (< 0.1 J/mol-K) are not significant over the temperature range studied, so $C_v \approx C_p$. The heat capacities calculated from the Kieffer models show excellent agreement with calorimetric data. For YPO_4, the calculated value of C_v =100.8 J/mol-K at 300 K shows excellent agreement with the data of Gavrichev et. al.[21] who reported a value of C_p = 99.25 J/mol-K at 298.4 K. For $CePO_4$, the calculated value of C_v =109.4 J/mol-K at 300 K also shows very good agreement with the data of Perriere et. al.[22] who reported a value of C_p = 110 J/mol-K at 323.15 K. This data can also be compared with values from Thiriet et. al.[23] who measured heat capacity experiments on synthetic $CePO_4$ and determined a value of 106.43 J/mol-K at 298.15 K. The published values are within 1-3% of the heat capacities calculated with the Kieffer model and therefore give confidence to using these models in more extended thermodynamic calculations.

Table 2.6 Calculated Heat Capacity Values for YPO_4

Temperature (Kelvin)	*Acoustic Heat Capacity Cont. (J/mol*K)*	*Optic Heat Capacity Cont. (J/mol*K)*	*Einstein Heat Capacity Cont. (J/mol*K)*	*Total Heat Capacity, Cv (J/mol*K)*
0	0	0	0	0
100	10.23	17.74	0.01	27.99
200	11.86	51.71	2.23	65.79
300	12.18	76.99	11.63	100.80
400	12.29	84.53	23.44	120.28
500	12.36	90.69	32.68	135.73
600	12.40	96.08	40.84	149.32
700	12.40	96.67	45.41	154.47
800	12.42	100.33	49.87	162.62
900	12.43	100.75	52.72	165.89
1000	12.45	100.75	55.41	168.60

Table 2.7 Calculated Heat Capacity Values for $CePO_4$

Temperature (Kelvin)	*Acoustic Heat Capacity Cont. (J/mol*K)*	*Optic Heat Capacity Cont. (J/mol*K)*	*Einstein Heat Capacity Cont. (J/mol*K)*	*Total Heat Capacity Cv (J/mol*K)*
0	0	0	0	0
100	5.71	30.58	0.00	36.29
200	6.10	80.14	1.23	87.47
300	6.17	97.19	6.01	109.38
400	6.20	111.33	12.04	129.57
500	6.21	112.17	16.71	135.09
600	6.21	117.71	20.42	144.35
700	6.22	122.68	23.08	151.98
800	6.22	122.68	25.29	154.19
900	6.22	122.68	26.36	155.26
1000	6.22	122.68	27.70	156.61

2.4 Conclusion

This chapter presented results of the Raman spectroscopic data that has been collected for this dissertation on rare-earth phosphate minerals. Raman spectra collected under ambient conditions for $GdPO_4$ and $CePO_4$ monazite are compared with $ScPO_4$ and YPO_4 xenotime. The difference in the natural sample of $CePO_4$ and the synthetic sample of $GdPO_4$ is discussed. All of the spectra collected show excellent agreement with the previous studies.[7-9] High pressure Raman data are presented for $GdPO_4$ and $ScPO_4$ and show that no phase transitions occur between 1 bar and 10 GPa. The high pressure data indicate that the lattice modes of $GdPO_4$ remain essentially invariant with pressure and the greatest shifts are seen by the internal PO_4 stretching modes. For $ScPO_4$, similar trends of the internal PO_4 modes are observed with the exception of a lattice mode showing a slight decrease with pressure. The spectroscopic data was used to develop Kieffer lattice vibrational models from which isochoric heat capacities were calculated from 0 K to 1000 K temperature. The heat capacities agree within 1-3% of experimental data and confirm that the Kieffer model provides an effective method for calculating heat capacities and other thermodynamic data from lattice vibrational spectra of phosphate minerals.

References

[1] Williams, Q. *Min. Phys. And Cryst.* **1995**, *95*, 291−302.

[2] Kieffer, S. W. *Reviews of Geophysics* **1979**, *17*, 1−19.

[3] Kieffer, S. W., *Reviews of Geophysics* **1979,** *17*, 20−34.

[4] Kieffer, S. W. *Reviews of Geophysics* **1979**, *17*, 35−59.

[5]Kieffer, S. W. *Reviews of Geophysics* **1980**, *18*, 862−886.

[6] Kieffer, S. W. *Reviews of Geophysics* **1982**, *20*, 827−849.

[7] Begun, G. M.; Beall, G. W.; Boatner, L. A.; Gregor, W. J. *J. Raman Spec.* **1981**, *11*, 273−278.

[8] Silva, E. N.; Ayala, A. P.; Guedes, I.; Paschoal, C. W. A.; Moreira, R. L.; Loong, C. K.; Boatner, L. A. *Optic. Mater.* **2006**, *29*, 224−230.

[9] Giarola, M.; Sanson, A.; Rahman, A.; Mariotto, G.; Bettinelli, M.; Speghini, A.; Cazzanelli, E. *Phys. Rev. B.* **2011**, *83*, 224302.

[10] DeAngelis, B. A.; Newnham, R. E.; White, W. B. *Am. Min.* **1972**, 57, 255−268.

[11] Speciale, S.; Marquardt, H.; Duffy, T. S. "*Brillouin scattering and its application in Geosciences"* in: *Spectroscopic Methods in Minerology and Material Sciences*, *Rev. in Mineralogy and Geochemistry*, Henderson, G. S.; Neuville, D. R.; Downs, R. T. (Eds.),Vol. 78, Mineralogical Society of America & the Geochemical Society, **2014**.

[12] Ferraro, J. R.; *Appl. Spec.* **1975**, *29*, 418−421.

[13] Boatner, L. A.; "*Structure and Properties of Monazite, Pretulite and Xenotime"* in: *Phosphates: Geochemical, Geobiological, and Materials Importance*, *Rev. in Mineralogy and Geochemistry*, Hughes, J. M.; Kohn, M.; Rakovan, J. (Eds.), Vol. 48, Mineralogical Society of America & the Geochemical Society, **2002**.

[14] Mao, H. K.; Bell, P. M.; Shaner, J.W.; Steinberg, D. J. *J. Appl. Phys.* **1978**, *49*, 3276–3283.

[15] Angel, R.J.; Bujak, M.; Zhao, J.; Diego Gatta, G.; Jacobsen, S. D. *J. Appl. Cryst.* **2007**, *40*, 26–32.

[16] Ruschel, K.; Nasdala, L.; Kronz, A.; Hanchar, J. M.; Többens, D. M.; Škoda, R.; Finger, F.; Möllen, A. *Mineral. Petrol*. **2012**, *105*, 41–55.

[17] Chopelas, A. *Am. Mineral.* **1991**, *76*, 1101–1109.

[18] Mogilevsky, P.; Zaretsky, E.B.; Parthasarathy, T.A.; Meisenkothen, F. *Phys. Chem. Miner.* **2006**, *33*, 691–698.

[19] Lacomba-Perales, R.; Errandonea, D.; Meng, Y.; Bettinelli, M. *Phys. Rev. B.* **2010,** *81,* 064113.

[20] Feng, J.; Xiao, B.; Zhou, R.; Pan, W. *Acta Mater*. **2013**, *61,* 7364–7383.

[21] Gavrichev, K. S.; Ryumin, M. A; Tyurin, A. V.; Gurevich, V. M.; Komissarova, L. N. *Geochem. Inter.* **2010,** *48*. 932–939.

[22] Perriere, L.; Bregiroux, D.; Naitali, B.; Audubert, F.; Champion, E.; Smith, D. S.; Bernache-Assollant, D. *J. Eur. Cer. Soc.* **2007.** *27*. 3207–3213.

[23] Thiriet, C.; Konings, R .J. M.; Javorský, P.; Wastin, F. *Phys. Chem. Miner.* **2004**, *31*, 347–352.

Chapter 3: Equation of State of Rare-Earth Phosphates

3.1 Introduction

An equation of state (EoS) describes the relationship between the state of a material and certain physical parameters. In this study, appropriate EoS models were used to define the mathematical relationship between pressure and volume of rare-earth phosphate minerals. More specifically, these models were used to determine the bulk moduli of these minerals, and to quantify their resistance to uniform compression. The bulk modulus is a thermodynamic property that gives information about the stability of a material. It is particularly important to the study of earthquakes and in aiding our understanding of how crustal minerals will react to high levels of energy.[1] Bulk moduli are measured in pressure units, and most mineral samples have values between ~20 GPa and ~400 GPa. For reference, diamond, being one of the most rigid materials known to man, lies at the high end of this spectrum with a bulk modulus of 442 GPa.[2]

3.1.1 Background

Within the rare-earth phosphate mineral group, the ionic radius of the lanthanide cation causes more than a change in crystal structure; it also affects the elastic properties of the material. This chapter focuses on determining the EoS and bulk moduli for the natural $CePO_4$ and the synthetic $GdPO_4$ monazite samples and the synthetic $TbPO_4$, and $ScPO_4$ xenotime samples.

Previous high-pressure studies on these materials focused on determining the elastic properties and on inducing phase transitions between the structure types. However, most of these previous works were preformed on powder samples and the experiments were conducted to extremely high pressures, producing non-hydrostatic pressure conditions. These experimental factors reduce the reliability of the data. This uncertainty arises because EoS calculations require high precision in the determination of the unit cell parameters, which is not feasible with high-pressure powder diffraction methods because the width of the diffraction peaks increases the uncertainty of peak positions. Also, non-hydrostatic conditions can create *unquantified* shear stresses on the materials causing unreliable results.[3] This is especially important as rare-earth phosphate minerals are known to be particularly sensitive to shear stresses. Pressure media that

were used in previous studies included a 4:1 methanol/ethanol mixture and neon. These media have hydrostatic limits of 9.8 GPa and 15 GPa respectively.[4,5] Within these studies, phase transitions were observed between 9.5 GPa and up to 60 GPa.[6-10] At such high pressures the shear stresses on the minerals make it much harder to determine what effects are directly due to pressure, and which ones are caused by shear forces. These studies do suggest a general trend that increasing rare-earth cationic radius is associated with decreasing bulk modulus, but the scatter in the data does not allow for any definitive conclusions to be drawn (Figure 3.1). This issue will be discussed in more detail later in this chapter. Table 3.1 summarizes previously published bulk moduli for materials of interest to this study.

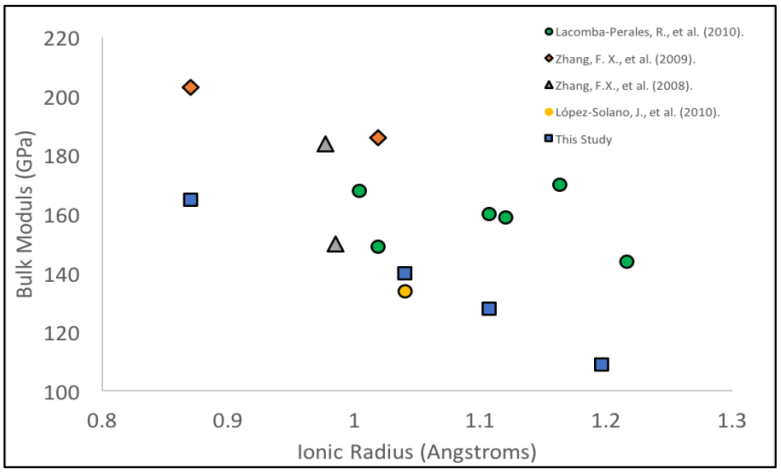

Figure 3.1 Published Bulk Moduli vs. Ionic Radii: Bulk moduli vs. Ionic Radii plot comparing four sets of published data (ref. [6][7][8][9]) with data obtained in this study.

Table 3.1 Published Bulk Moduli Data for Monazite and Xenotime Materials.

Mineral	*Bulk Modulus (GPa)*	*Reference*
YPO_4 (xenotime)	149(2)	[6]
$ErPO_4$ (xenotime)	168(4)	
$GdPO_4$ (monazite)	160(2)	
$EuPO_4$ (monazite)	159(2)	
$NdPO_4$ (monazite)	170(2)	
$LaPO_4$ (monazite)	144(2)	
$ScPO_4$ (xenotime)	203(7)	[7]
YPO_4 (xenotime)	186(5)	
$TbPO_4$ (xenotime)	134*	[8]
$YbPO_4$ (xenotime)	150(5)	[9]
$LuPO_4$ (monazite)	184(4)	
$CePO_4$ (monazite)	109(1)	[18]

3.1.2 Equation of State Theory

In high pressure diffraction work, the EoS describes changes to a material's unit cell parameters in response to pressure. By quantifying these relationships isothermal elastic constants such as the bulk modulus and axial compressions can be calculated. There are several empirical EoS models available for modeling high pressure diffraction data, namely, the Murnaghan, Natural Strain, Vinet, and Birch-Murnaghan models.[11] The model most suitable for a given set of data depends on the response of the material to pressure. The Murnaghan EoS is dependent on the bulk modulus and pressure having a linear relationship, and can only correctly fit pressure and volume data if the volume change is 10% or less of the original volume. The Natural Strain EoS is based upon a linear expression for the natural strain. It is mathematically similar to the Birch-Murnaghan EoS, but the elastic constants calculated from the Natural Strain EoS tend to be less reproducible that those determined with the Birch-Murnaghan model. The Vinet EoS is commonly used for samples for which the unit cell compression is very high - typically more than about 60% of the original volume. The most universally applicable EoS is the Birch-Murnaghan (BM-EoS), which has been successfully applied in modeling a wide range of compressional behavior, and is the EoS used to deduce the elastic constants of the materials discussed herein.

The BM-EoS incorporates the Eulerian strain, f_e:

$$fe = \frac{\left(\frac{V_0}{V}\right)^{\frac{2}{3}} - 1}{2}$$

where V_0 = unit cell volume at ambient pressure; V = volume at pressure, P. The BM-EoS can be expanded to first, second, third, and fourth order with respect to f_e, the fourth order expansion is as follows: [10]

$$P = 3K_0 * fe(1 + 2fe)^{\frac{5}{2}} * [1 + \frac{3}{2}(K' - 4) * fe + \frac{3}{2}\left(K_0 * K'' + (K' - 4)(K' - 3) + \frac{35}{9}\right) * fe^2]$$

The third order truncation of the BM-EoS sets the f_e^2 coefficient to zero by forcing K'' to equal a value that ensures this outcome. Consequently, the 3rd order BM-EoS includes only the variables V, V_0, K_0, and K'.

The terms K_0 and K' in the BM-EoS are defined as follows:[11]

$$K_0 = -V * \frac{\partial P}{\partial V} \qquad \text{and} \qquad K' = \frac{\partial K_0}{\partial P}$$

For all experiments in this work, the bulk moduli are considered to be isothermal and are measured in gigapascals (GPa) as this is the unit most commonly employed for reporting K_0 values of minerals.

One of the most useful ways to visualize EoS information is to plot the data as finite strain vs. normalized stress (a so-called f-F plot), where in the BM-EoS finite strain is equivalent to the Eulerian strain, f_e, and the normalized stress is given by

$$F_E = \frac{P}{3 * fe(1 + 2fe)^{\frac{5}{2}}}$$

This visualization method is helpful for determining which order of EoS is provides the most appropriate fit to the experimental data. An example is shown in Figure 3.2. This figure shows the f-F plot for $ScPO_4$, and 2nd, 3rd and 4th order BM-EoS fits to the data. Table 3.2 provides the elastic constants for this material derived from these fits. It is clear that both the 3rd and 4th order fits visually match the data. However, consideration of the estimated standard deviation (esd) values associated with the elastic constants, indicate that the 4th order fit results in over-parameterization of the data. Therefore, the 3rd order BM-EoS fit to the $ScPO_4$ data is most appropriate in this case. Indeed, a 3rd order BM-EoS model was found to be the most acceptable model for the compressional data for all the rare-earth phosphate samples investigated.

Table 3.2 Elastic Constants for $ScPO_4$ Calculated from 2nd, 3rd, and 4th order Fits to the f-F Data.

Elastic constant	*2nd order BM-EoS*	*3rd order BM-EoS*	*4th order BM-EoS*
V_0 (Å^3)	250.584(19)	250.634(10)	250.636(12)
K_0 (GPa)	173.8(7)	166.1(11)	165(2)
K'	4.000	6.7(4)	7.6(19)
K''(GPa^{-1})	−0.02238	-0.08200	−0.4(8)

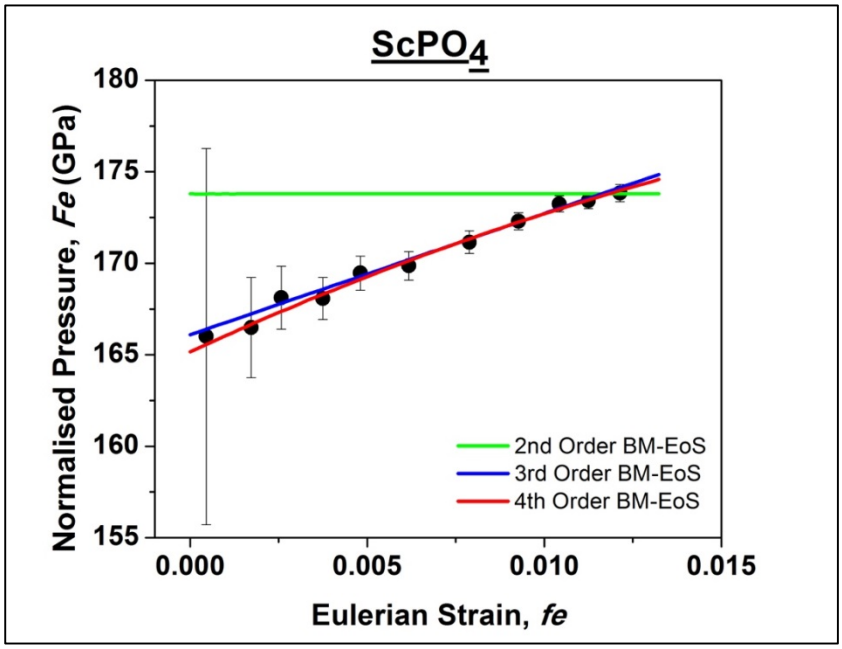

Figure 3.2: $ScPO_4$ f-F Plot. Also shown are 2nd, 3rd and 4th BM-EoS fits to the data.

3.2 Experimental Methods

3.2.1 Samples

High-pressure EoS determinations were performed on a suite of rare-earth phosphate minerals including $CePO_4$, $GdPO_4$, $TbPO_4$, and $ScPO_4$. The $GdPO_4$, $TbPO_4$, and $ScPO_4$ samples were synthesized via a high-temperature solution growth method by Lynn Boatner at Oak Ridge National Laboratory (TN, USA). This process takes over two months and is described in more detail in "Structure and Properties of Monazite, Pretulite and Xenotime," in: *Phosphates: Geochemical, Geobiological, and Materials Importance*.[12] The $CePO_4$ sample used in this investigation was naturally sourced from a mine located in Hiddenite, North Carolina. The bulk rock composition from which this sample was extracted is of a Pre-Cambrian gneiss, and $CePO_4$ monazite forms as small honey colored crystals in the cavities of the pegmatite and are ingrained in calcite and/or albite crystals.[13] Microprobe analyses give a chemical composition of $Ce_{0.44}La_{0.21}Nd_{0.18}Pr_{0.06}Gd_{0.04}Th_{0.03}Sm_{0.02}Ca_{0.01}Y_{0.01}(P_{0.98}Si_{0.02}O_4)$, but for convenience this sample will be denoted as $CePO_4$ in this thesis. This composition was determined on a Cameca SX-50 Electron Probe Microanalyzer with a label set to analyze for P, Si, Th, Y, La, Ce, Pr, Nd, Gd, U, Ca, and Sm. The sample grain was mounted and polished before being loaded into the probe. The sample was analyzed for 50 runs over 500μm, which took about 3.5 h.

3.2.2 High-Pressure X-Ray Diffraction

Single crystals of $CePO_4$, $GdPO_4$, $TbPO_4$, and $ScPO_4$ were cut to appropriate size of about 80 × 140 × 180 μm^3, and loaded separately into a sample chamber (approximately 290 × 100 μm^2 in size) that was drilled into a steel gasket that was fitted in a standard ETH diamond anvil cell (DAC).[14] A quartz crystal was also loaded into the cell along with the sample crystal to act as a pressure calibrant.[15] Quartz makes a particularly good pressure calibrant as its high pressure behavior, including accurate elastic constants, are well known. Therefore, the pressure in the cell can be calculated very accurately and precisely from the relative change in the unit cell volume of the quartz crystal. Diffraction data were first collected under ambient conditions before a 4:1 MeOH:EtOH mixture was added to the DAC. This mixture acts as a pressure-transmitting medium and is known to ensure a hydrostatic environment in the DAC up to 9.8 GPa.[4]

Precise unit cell parameters for the sample and quartz crystals were obtained from data collected on a Huber diffractometer equipped with a Eulerian cradle, a point detector, and operating with MoK_α radiation (λ = 0.71073 Å). The method is based on the 8-position centering of 10 − 25 intense diffraction maxima within the $9° < 2\theta < 33°$ range.[16] Table 3.3 shows the various crystal sizes and constrained unit cell parameters recorded under ambient conditions for each sample. Unit cell parameters were collected at 0.5 − 1.0 GPa intervals. These parameters were plotted against pressure, and the resulting curves were fit by a least-squares technique with 3rd order BM-EoS experessions[11] from which bulk moduli data were calculated. These calculations were done in EoSFit 7.0.[17] Esd values for the calculated constants were determined by weighting the fit to the measured uncertainties of the data.

Table 3.3: Crystal Size and Constrained Unit Cell Parameters for the Phosphate Samples Employed in this Study. These parameters were recorded at room pressure. M = monazite (monoclinic); X = Xenotime (tetragonal).

Mineral	*Crystal Size (μm^3)*	*a-axis (Å)*	*b-axis (Å)*	*c-axis (Å)*	*β angle (o)*	*Volume ($Å^3$)*
$CePO_4$ (M)	109 ×134 × 181	6.4896(3)	7.0224(2)	6.8162(3)	103.687(3)	301.81(2)
$GdPO_4$ (M)	81 × 153 × 248	6.3358(1)	6.8484(2)	6.6519(2)	104.023(2)	280.02(2)
$TbPO_4$ (X)	110 × 151 × 172	6.9427(1)	--	6.07094(9)	--	292.63(1)
$ScPO_4$ (X)	52 × 64 × 106	6.5769(2)	--	5.7943(2)	--	250.64(1)

3.3 Results and Discussion

3.3.1 Natural vs. Synthetic Samples

In this section the EoS for the natural $CePO_4$ sample used in this study is compared with previously published data for a synthetic $CePO_4$ sample.[18] Huang et. al. prepared single crystals of $CePO_4$ by a flux method.[18] A single crystal of synthetic $CePO_4$ was loaded into a DAC along with gold powder (pressure calibrant) and a 4:1 MetOH:EtOH mixture was used as the pressure medium. The results of this published study are shown in Figure 3.3 alongside the results of this study. The curves shown in Figure 3.3 are almost identical, and the reported bulk modulus, K_0, for the synthetic sample, 109(1) GPa, concurs with the value of 109(3) GPa measured for the natural $CePO_4$ sample employed in this study. Therefore, the difference between the EoS for natural and synthetic samples is negligible, despite the large degree of cation substitution in the natural sample. Accordingly, the conclusions presented in the remaining part of this chapter, which were deduced from studies on synthetic materials, still present meaningful data for geologic modeling purposes.

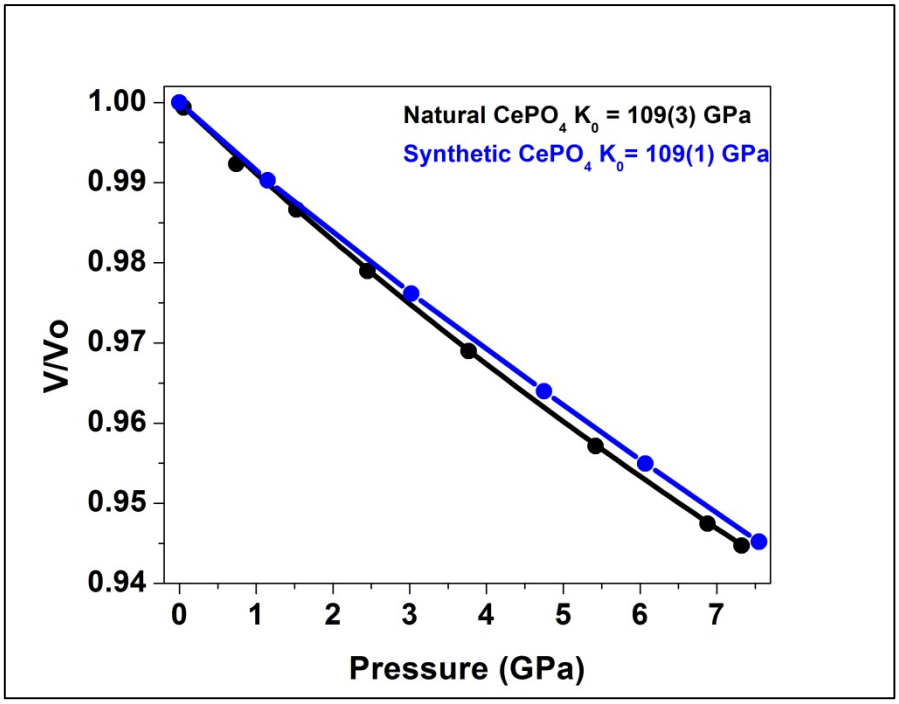

Figure 3.3: Relative Volume vs Pressure Data for Natural and Synthetic $CePO_4$. Data for the synthetic sample were taken from ref. [17]. Both sets of data were fitted with 3rd order BM-EoS. The BM-EoS fits are shown in blue and black for the synthetic and natural sample, respectively.

3.3.2 Elastic Constants

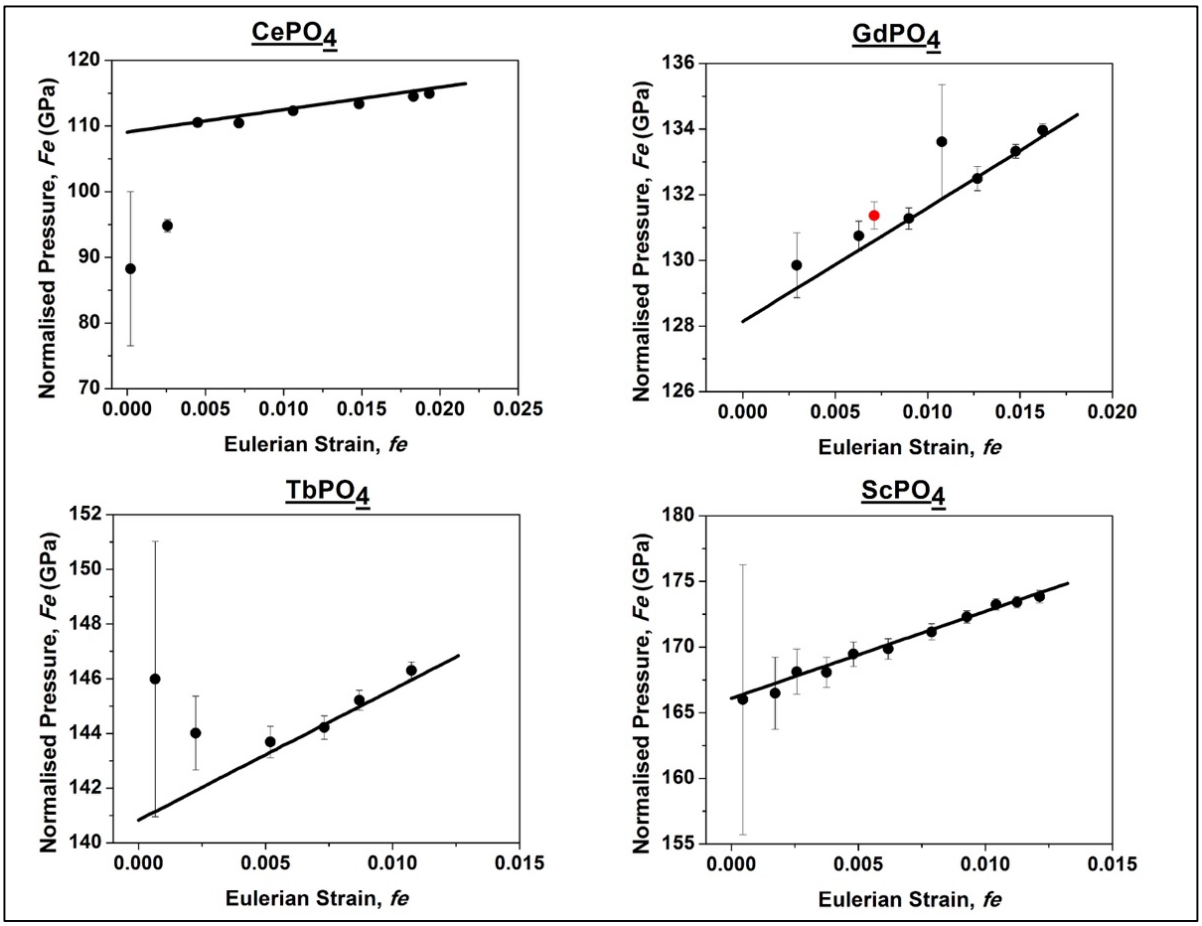

Figure 3.4 f-F Plots. f-F plots for all samples included in this study; experimental data are shown as circles, black and red circles represent data collected during pressure increase and decrease, respectively. Black lines represent 3rd order BM-EoS fits to the data. Error bars are included for all experimental data, but in some cases are smaller than the symbol.

The f-F plots for all samples covered in this study are shown in Figure 3.4, each set of data have been fit with a 3rd order BM-EoS. f-F plots are sensitive to small deviations from the expected volume/pressure relationship and commonly used to detect phase transitions. The plots for these studies show that no phase transitions took place over the pressure ranges investigated. That said, for $CePO_4$ the 3rd order BM-EoS fit provides a reasonable fit to all data points within error except for the second data point (f_e = 0.0002, P = 0.055(2) GPa). The deviation of the data from the BM-EoS line may indicate that there was a possible phase transition between 0.055(2) and 0.742(2) GPa. However, evaluation of the structural data recorded at various pressure points,

including at pressures > 0.742(2) GPa indicate no such transition occurring.[§] Furthermore, the unit cell data (vide infra) are also consistent with no such transition taking place. Furthermore, a plot of the relative change in unit cell volume with pressure (Figure 3.5) shows that the corresponding data point at P = 0.055(2) GPa slightly deviates from EoS fit, even though all subsequent points fit the BM-EoS curve perfectly – an effect that is exaggerated in the f-F plot. The anomalous behavior of this data point is most likely due to experimental error, such as the environment in the DAC not reaching equilibrium before the data were collected.

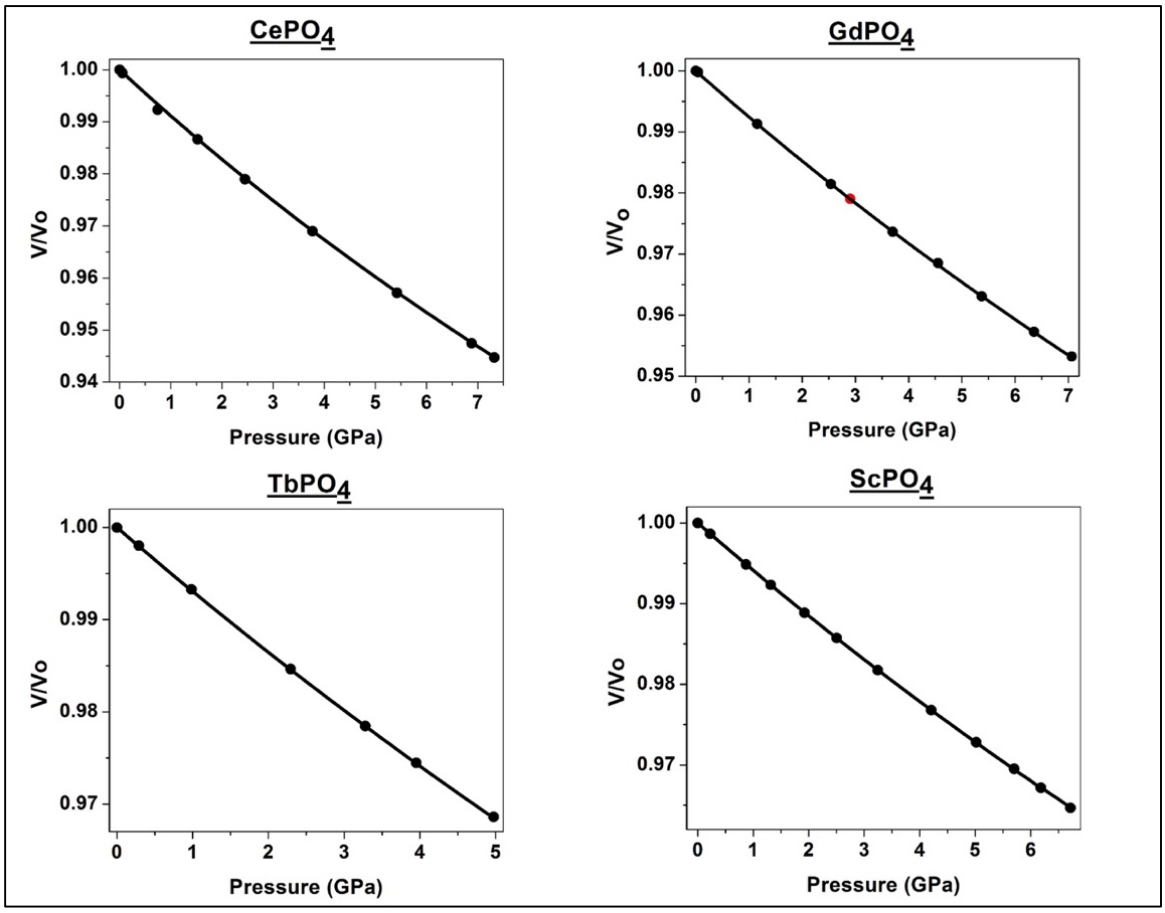

Figure 3.5 V/V_0 vs. Pressure Plots. Relative volume vs pressure plots for all samples included in this study; experimental data are shown as circles, black and red circles represent data collected during pressure increase and decrease, respectively. Black lines represent 3rd order BM-EoS fits to the data. Error bars are included for all experimental data, but in some cases are smaller than the symbol.

[§] Unfortunately these data are of insufficient quality for publication or inclusion in this thesis.

For $GdPO_4$, and $ScPO_4$ the 3rd order BM-EoS fits to the data are good and accurately model the all data points. Higher order BM-EoS models were tried for these datasets but resulted in over parameterization of the data. Conversely, the $TbPO_4$ plot shows discrepancies: the 3rd order BM-EoS does not appear to represent the low pressure ($f_e < 0.0025$, P < 0.3 GPa) data well, and indeed a 4th order BM-EoS was applied to the data and visually appeared to give a more acceptable fit. Nonetheless, importantly, the esd values on the calculated elastic constants (K′ = 2(2) and K″ = 2(1) GPa^{-1}) indicated that this higher order model significantly over parameterizes the data. Conversely, despite the 3rd order model providing a less visually appealing fit it does provide more acceptable elastic constants (Table 3.5), and was therefore the final model chosen for this data.

Figure 3.5 displays the relative unit cell volume vs. pressure plots for all the samples in this study. These plots confirm that no phase transitions occurred for any sample over the investigated pressure ranges. These graphs also provide a visual representation of the compression of the samples, which is inversely related to their K_0 values (Table 3.5). It is evident from the bulk moduli and the curves in Figure 3.5 that both the xenotime and monazite structures are relatively incompressible; to place these values in geological context, bulk moduli of feldspar minerals that comprise approximately 60% of the Earth's crust usually fall within the range of $50 < K_0 < 80$ GPa[19-21]

Table 3.4 Elastic Constants for the Phosphate Samples Employed in this Study. These constants were calculated from 3rd order BM-EoS fits to pressure vs. volume data. M = monazite; X = xenotime.

Elastic Constants	*$CePO_4$ (M)*	*$GdPO_4$ (M)*	*$TbPO_4$ (X)*	*$ScPO_4$ (X)*
V_0 (Å^3)	301.81(2)	280.02(2)	292.64(1)	250.64(1)
K_0 (GPa)	109(3)	128.1(8)	141(1)	166(1)
K′	6.1(10)	5.8(2)	6.3(5)	6.7(4)

It is immediately clear that the K_0 values for $GdPO_4$, $TbPO_4$, and $ScPO_4$ measured in this study are notably different from those reported in the literature (Table 3.1). This a consequence of the widely differing experimental conditions under which the high pressure diffraction data were collected. Indeed, our results for $ScPO_4$ provide an excellent example of the importance of understanding the strain conditions within a DAC when evaluating the elastic constants for a material. Zhang et al. collected high pressure powder diffraction data on the xenotime phase of

$ScPO_4$ up to ~30 GPa with "*standard methanol/ethanol with or without water*".[7] These authors state that this pressure medium remains hydrostatic below 10 − 12 GPa. If we assume that the "standard" alcohol mixture they are referring to is 4:1 MeOH/EtoH then the hydrostatic limit is known to be 9.8 GPa.[4] At pressures above this limit, the sample is subject to deviatoric stresses induced by shear forces that can alter the crystal structure. Such effects can induce phase transitions, and importantly from our perspective, seriously affect the elastic constants derived from diffraction data collected under such conditions.[3] As the stress state in the DAC is often unknown when the hydrostatic regime is deviated from, elastic constants determined under these conditions are unreliable and often irreproducible. This explains why Zhang's K_0 value of 203(7) GPa is so drastically different from our value of 166(1) GPa determined under hydrostatic conditions. Further credence to this explanation is given in section 3.3.1 in which results from two separate determinations of the elastic constants for $CePO_4$ are compared. In this case both single crystal samples were evaluated under similar stress conditions and consequently the calculated K_0 values are the same. Furthermore, non-hydrostatic conditions were employed in the previous K_0 determination of $GdPO_4$ in which data were collected up to ~30 GPa with neon as the pressure transmitting medium (hydrostatic limit of 15 GPa).[5]

In the case of $TbPO_4$ the extent of disagreement between the K_0 values reported by López-Solano et al. (134 GPa) and the value of 141(1) GPa determined in this study is impossible to evaluate as these authors do not provide an associated esd value.[8] However, their diffraction data were collected under hydrostatic conditions, but on a powdered sample. As powder diffraction does not provide unit cell parameters with the same high level of precision as single crystal methods, it is possible that this is the cause of the difference between our two K_0 values.

Table 3.5 Axial Moduli for the Phosphate Samples Employed in this Study. These constants were calculated from 3rd order BM-EoS fits to pressure vs. unit cell axis length data. M = monazite; X = xenotime

	$CePO_4$ (M)	***$GdPO_4$ (M)***	***$TbPO_4$ (X)***	***$ScPO_4$ (X)***
		M_0 (GPa)		
a-axis	430(12)	463(3)	335(3)	391(3)
b-axis	322(9)	389(3)	--	--
c-axis	241(6)	297(2)	871(10)	1065(17)

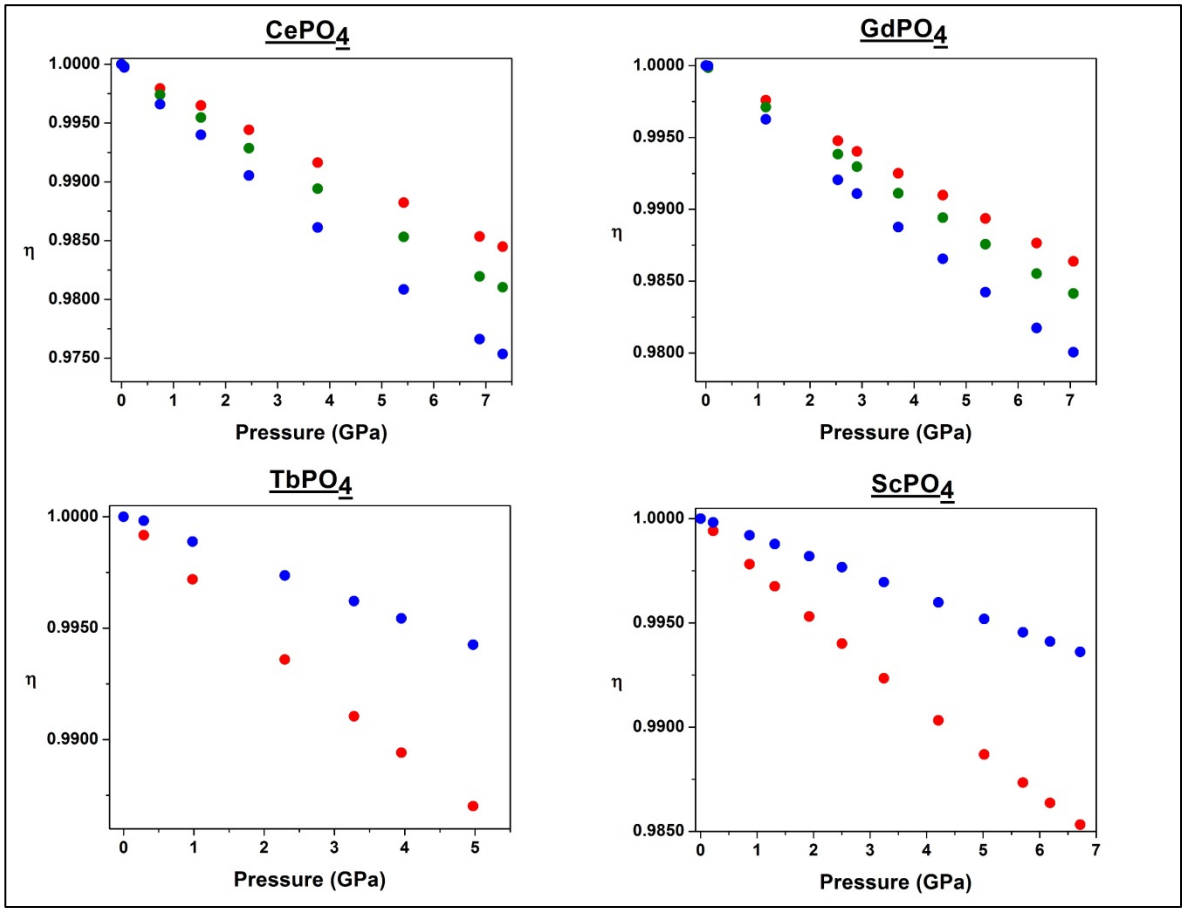

Figure 3.6 Normalized Unit Cell Axes Lengths vs. Pressure Plots. Normalized unit cell axes lengths vs. pressure plots for all samples included in this study. Red: *a*-axis; green: *b*-axis; blue: *c*-axis. Error bars are included for all experimental data, but are smaller than the symbols.

Figure 3.6 shows the individual axial compressions for each rare-earth phosphate sample, and the associated axial moduli (M_0) are reported in Table 3.6. As compressibility is inversely related to the axial modulus, the smaller the M_0 value for an axis the more compressible the structure is in that direction. For the monazite

e samples ($CePO_4$ and $GdPO_4$) the axial compressibilities are in the order [100] < [010] < [001]; for the xenotime samples ($TbPO_4$, and $ScPO_4$) the order is [001] << [010]=[100], indicating that the structure is more compressible parallel to the *ab* plane than along the *c*-axis.

The monazite and xenotime structures display different compressional trends: in monazite the structure is most compressible along the *c*-axis, but in xenotime the *ab*-plane is the most compressible. These differences are related to structural differences between monazite and xenotime. For both crystal systems the packing arrangement of the polyhedra is described as chains of alternating PO_4 and $REEO_x$ (x = 8 for xenotime, and x = 9 for monazite) polyhedra. For

monazite, these chains lie parallel to the [100] direction and for xenotime they lie parallel to the [001] direction (see Chapter 1 for a more in-depth structural descriptions).[22] In both structure types, the M_0 values suggest that compression is easier in the directions perpendicular to these chains, and is hindered in the directions in which the chains lie parallel. It is clear that the chains confer rigidity to the structures. Furthermore, the compressibilities of the *c*-axes reported in Table 3.6 are inversely proportional to the size of the lanthanide cation i.e. the smaller the cation, the less compressible the *c*-axis is. This indicates that the lanthanide polyhedra play a role in the compression mechanisms operating in these materials; this issue is discussed in more detail in Chapter 4.

3.3.3 Bulk Moduli vs. Cation Radii

In this study all high-pressure data were collected under the same hydrostatic conditions, which allows for direct comparison of the results, and confidence that elastic constants derived from these data are reliable. The data obtained for the two monazite samples ($CePO_4$, and $GdPO_4$) and two xenotime samples ($TbPO_4$ and $ScPO_4$), can be used to better understand the relationship of bulk moduli within the mineral groups, and across the phase boundary. Figure 3.7 shows a plot of the measured bulk moduli of all minerals analyzed in this study verses the ionic radii of their rare-earth cations (Shannon and Prewitt Radii).[23] This plots show a linear relationship between these two parameters, which holds across the monazite/xenotime boundary. This trend supports the hypothesis that samples with the monazite structure, which contain the larger rare-earth cations, will be easier to compress than xenotime structures that incorporate smaller cations. Since this trend holds across the monazite/xenotime boundary, it seems that the structure type has little to no effect on the bulk modulus of these minerals and depends solely on the particular rare-earth cation present. However, this finding is based on only four data points, and further studies are required before definitive conclusions are made.

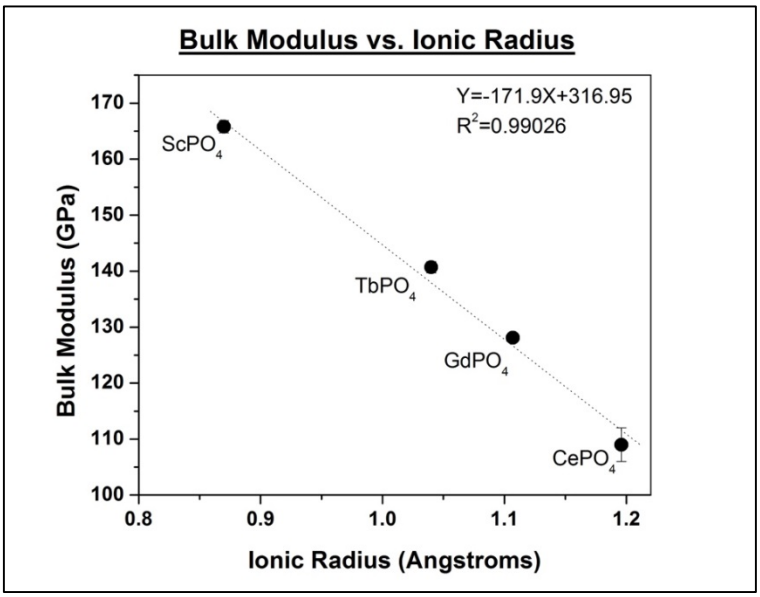

Figure 3.7 Ionic Radii vs. Bulk Moduli. This plot displays the relationship between experimental bulk moduli and rare-earth cation radii for the rare-earth phosphates in the study. The dashed line represents the linear regression fit to the data. Errors are included, but smaller tan data point for some samples.

Table 3.6 Calculated Bulk Moduli for Selected Phosphates. Ionic radii are from reference [23].

Mineral	*Ionic Radius (Å)*	*Calculated K_0 (GPa)*
YPO_4 (xenotime)	1.019	141.8
$LuPO_4$ (xenotime)	0.977	149.0
$YbPO_4$ (xenotime)	0.985	147.6
$HoPO_4$ (xenotime)	1.015	142.5
$EuPO_4$ (monazite)	1.12	124.4
$SmPO_4$ (monazite)	1.079	131.5
$NdPO_4$ (monazite)	1.163	117.0
$LaPO_4$ (monazite	1.216	107.9

It is also noteworthy that the data in Figure 3.7 displays less scatter than the equivalent plot displaying previously published data (Figure 3.1), which has allowed for a mathematical relationship between K_0 and cation radii to be determined for these monazite/xenotime materials: a linear regression fit to the experimental data in Figure 3.6 (R^2 = 0.99026) gives the following expression:

$$\text{Bulk modulus} = (-171.9 \times \text{Ionic Radius}) + 316.95$$

This equation can be used to predict bulk moduli for all other rare-earth phosphates. A select number of these calculated bulk moduli are show in Table 3.6. These calculated K_0 values assume that the monazite/xenotime is subject to hydrostatic pressure, and consequently cannot be

compared legitimately to the values in Table 3.1 that were derived from diffraction data collected under a variety of non-hydrostatic conditions.

3.4 Conclusion

A systematic EoS study of four rare-earth phosphate minerals, two monazite ($CePO_4$ and $GdPO_4$), and two xenotime ($TbPO_4$ and $ScPO_4$), has been presented in this chapter. Three of these samples were synthetic and one was natural ($CePO_4$). Elastic constants, e.g. bulk and axial moduli, were calculated for all the samples in this study by 3rd order BM-EoS fits to the pressure-dependent unit cell parameter data. In all cases, the data confirmed that no phase transitions occurred within the investigated pressure ranges.

Comparison of the elastic constants for the natural $CePO_4$ sample with those reported for a synthetic sample indicated no statistical difference between the two K_0 values. This finding suggests that elastic constants determined for synthetic phosphate samples are similar to those for more chemically complex natural samples and can therefore be employed in geologic models.

There are significant discrepancies between the K_0 values for $TbPO_4$, $GdPO_4$ and $ScPO_4$ calculated in this study with previously published values. These are believed to have arisen due to differences in the experimental conditions to the samples were exposed. It is evident that mineral of this type are sensitive to shear forces, which severely affect their elastic behavior. Indeed, by conducting all experiments under hydrostatic conditions (i.e. no shear forces) the samples in this study were subject to the same experimental conditions and consequently a clear inverse linear relationship between K_0 and the ionic radii of the lanthanide has been seen. Conversely, because of the diverse experimental conditions employed in previous studies, these data exhibited a large degree of scatter, and no clear trend could be identified with certainty.

The axial moduli for the monazite and xenotime structures indicate these structures are most compressible in directions perpendicular to the PO_4/ReO_x chains, and least compressible in the direction parallel to the chains; this matter is discussed in more detail in the next chapter.

References

[1] "Bulk Elastic Properties". *Hyperphysics*. Georgia State University.

[2] Surratt, G. T. and Euwema, R. N. and Wilhite, D. L. *Phys. Rev. B.* **1973**, 8, 4019–4025.

[3] Zhao, J.; Angel, R .J.; Ross, N. L. *J. Appl. Cryst*. **2010**, *43*, 743–751.

[4] Angel, R. J.; Bujak, M.; Zhao, J.; Diego Gatta, G.; Jacobsen, S. D. *J. Appl. Cryst.* **2007**, *40*, 26–32.

[5] Klotz, S.; Chervin, J.-C.; Munsch, P.; LeMarchand, G. *J. of Phys. D: App. Phys.* **2009**, *42, 075413.*

[6] Lacomba-Perales, R.; Errandonea, D.; Meng, Y.; Bettinelli, M. *Phys. Rev. B.* **2010**, *81*, 064113.

[7] Zhang, F.X.; Wang, J. W.; Lang, M.; Zhang, J. M.; Ewing, R. C.; Boatner, L. A. *Phys. Rev. B.* **2009**, *81,* 184114.

[8] López-Solano, J, Rodriguez-Hernandez, P.; Munoz, A.; Gomis, O.; Santamaria-Perez, D.; Errandonea, D.; Manjon, F. J.; Kumar, R. S. Stavrou, E.; Raptis, C. *Phys. Rev. B.* **2010**, *81,* 144126.

[9] Zhang, F.X., Lang, M.; Ewing, R. C.; Lian, J.; Wang, Z. W.; Hu, J.; Boatner, L. A. *J. Sol. St. Chem.* **2008**, 2633–2638.

[10] Tatsi, A.; Stavrou, E.; Boulmetis, Y. C.; Kontos, A. G.; Raptis, Y. S.; Raptis, C. *J. Phys.: Cond. Matter.* **2008**, *20*, 425216.

[11] Angel, R. J.;.*High-Temperature and High-Pressure Crystal Chemistry*; Hazen, R. M.; Downs, R.T. (Eds).; Mineralogical Society of America, Washington, DC, **2000**; Vol. *41,* 35–59.

[12] Boatner, L. A.; "*Structure and Properties of Monazite, Pretulite and Xenotime"* in: *Phosphates: Geochemical, Geobiological, and Materials Importance*, *Rev. in Mineralogy and Geochemistry*, Hughes, J. M.; Kohn, M.; Rakovan, J. (Eds.), Vol. 48, Mineralogical Society of America & the Geochemical Society, **2002**.

[13] Palache, C.; Davidson, S. C.; Goranson E. A. *J. Min. Soc. Am.* **1927**, *15*, 280–302.

[14] Miletich, R.; Allan, D.R.; Kuh, W. F.; *High-Temperature and High-Pressure Crystal Chemistry*; Hazen, R. M., Downs, R. T. (Eds).; Mineralogical Society of America, Washington, DC, **2000**; Vol. *41,* 445–519.

[15] Angel, R. J.; Allen, D. R.; Miletich, R.; Finger, L. W. *J. Appl. Cryst.* **1997**, *30*, 461–466.

[17] Angel, R. J.; Gonzalez-Platas, J.; Alvaro, M. *Z. Kristallogr*. **2014**, *229*, 405–419.

[16] Angel, R. J.; Finger, L. W. *J. Appl. Cryst.* **2011**, *44*, 247–251.

[18] Huang, T.; Lee, J-S.; Kung, J.; Lin, C.-M. *J. Solid State Com.* **2010,** *150*, 1845–1850.

[19] Angel, R. J. *Contrib. Mineral Petrol.*, **2004**, *146*, 506–512.

[20] Downs, R. T.; Yang, H.; Hazen, R. M.; Finger, L. W. ; Prewitt, C. T. *Am. Mineral.* **1999**, *84*, 333–340.

[21] Benusa, M. D.; Angel, R. J.; Ross, N. L. *Am. Mineral.* **2005**, *90*, 1115–1120.

[22] Ni, Y.; Hughes, J. M.; Mariano, A. N. *Am. Min.* **1995**, *80*, 21–26.

[23] Shannon, R. D.; Prewitt, C. T. *Acta. Crystallogr.* **1969**, *B25*, 925.

Chapter 4: The Structural Response of Gadolinium Phosphate to Pressure

4.1 Introduction:

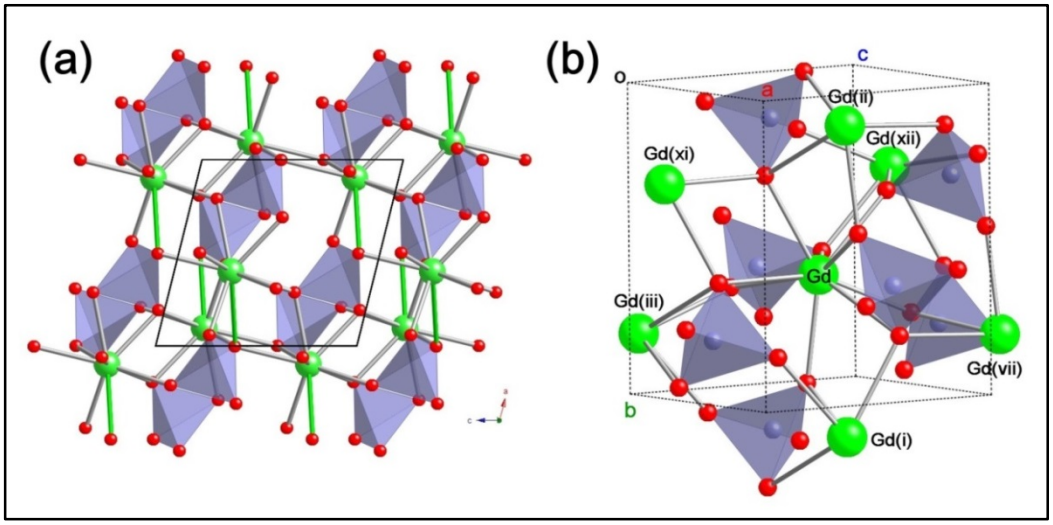

Figure 4.1:Crystal Structure of $GdPO_4$. (a) The crystal structure of $GdPO_4$ as viewed along the [010] direction; (b) the secondary coordination sphere of the Gd^{3+} ion in $GdPO_4$. Each ion is coordinated to seven PO_4 tetrahedra and has six edge-sharing interactions with neighboring Gd^{3+} ions. Green: Gd; red: O; light grey: P. Green struts represent the bond between Gd^{3+} ions and the capping oxygen atoms of the MCSAP, all other covalent bonds are shown in grey. Symmetry codes: (i) -x+1/2,y+1/2,-z+3/2; (ii) -x+1/2,y-1/2,-z+3/2; (iii) x-1/2,-y+3/2,z-1/2; (vii) x+1/2,-y+3/2,z+1/2; (xi) -x,1-y,1-z; (xii) –x, 1-y, 2-z.

As discussed in Chapter 3, many previous studies on rare-earth phosphate minerals focused on determining the elastic properties of MPO_4 compounds. However, the actual *structural response* of these materials to pressure remains underexplored. This important oversight must be addressed if these materials are to be used in practical applications. This chapter discusses the underlying changes in the crystal structure in response to hydrostatic pressure for a $GdPO_4$ monazite sample. Structural studies of this kind will lead to a greater understanding of the origins of the stability of general MPO_4 compounds and facilitate progress in their development for nuclear waste storage applications. As a monazite, $GdPO_4$ crystallises in the monoclinic space group $P2_1/n$. A complete review of the monazite structure at ambient conditions is presented in Chapter 1. Figure 4.1a (reproduced from Ch. 1 for reader convenience) and Figure 4.1b show a structural summary of $GdPO_4$. Fig. 4.1a shows the crystal structure

viewed along the [010] direction, and Fig. 4.1b shows the secondary coordination sphere, where each Gd^{3+} ion is coordinated to seven PO_4 tetrahedra, five vertex sharing and two edge sharing, and six Gd^{3+} polyhedra, all of which are edge sharing.

4.2 Experimental Method:

4.2.1 Synthesis

Single crystals of $GdPO_4$ were grown using a high-temperature solution (flux) growth method that has been described in detail previously.[1] For the growth of single crystals of $GdPO_4$, high-purity Gd_2O_3 was combined with lead hydrogen phosphate in a 50 ml platinum crucible that was then heated to 1360°C for several days. At 1360°C, lead pyrophosphate, $Pb_2P_2O_7$, forms via the decomposition of the lead hydrogen phosphate that then reacts with Gd_2O_3 to form $GdPO_4$ dissolved in a solution of molten $Pb_2P_2O_7$. Single crystals of $GdPO_4$ grow from the flux as the system is cooled to ~900°C. At this temperature, the growth furnace is rapidly cooled to room temperature, and the crystals are removed from the solidified flux by boiling the Pt crucible and growth charge in nitric acid for several weeks. The entire growth process requires a total period of over two months.

4.2.2 High-Pressure Diffraction

A single crystal of $GdPO_4$ ($81 \times 153 \times 248\ \mu m^3$) was loaded into a sample chamber approx. $290 \times 100\ \mu m^2$ in size that was drilled into a steel gasket that was fitted into a standard ETH diamond anvil cell (DAC).[2] A quartz crystal was loaded into the cell with the sample crystal to act as a pressure calibrant.[3] Diffraction data were first collected under ambient conditions, i.e. before a 4:1 MeOH:EtOH mixture was added to the DAC. This mixture acts as a pressure-transmitting medium and is known to remain hydrostatic up to 9.8 GPa.[4]

Data for structural analysis were collected at select pressures with an XCalibur-1 (Rigaku Oxford Diffraction) diffractometer equipped with a CCD detector and operating with monochromatic MoK_α radiation ($\lambda = 0.71073$ Å). The data were processed with standard instrument software. Sample and DAC absorption effects were corrected for with ABSORB-7.[5] Diamond dips and statistical corrections were performed with AVERAGE (R. J. Angel, 2003-2011). The high-pressure datasets were refined against the structure model determined from the crystal in air to obtain high-pressure models. This was possible because the

sample underwent no phase transitions over the pressure range investigated. Refinement was against F^2 by full-matrix least-squares refinement techniques. Due to restricted access to reciprocal space from the bulky DAC, datasets were not complete. With the reduced data:parameter ratio only the Gd ions could be refined ansiostropically. Key data and refinement parameter for the HP-XRD analysis are listed in Table 4.1.

Table 4.1. Data and Refinement Parameters for $GdPO_4$ as a Function of Pressure.

	~1 bar	**2.903(4) GPa**	**5.372(13) GPa**	**7.062(6) GPa**
Crystal system	monoclinic	monoclinic	monoclinic	monoclinic
Space Group	$P2_1/n$	$P2_1/n$	$P2_1/n$	$P2_1/n$
***a* (Å)**	6.33571(12)	6.29790(12)	6.26830(11)	6.24937(12)
***b* (Å)**	6.84840(17)	6.80019(19)	6.7632(2)	6.7397(2)
***c* (Å)**	6.6516(3)	6.5923(2)	6.5466(2)	6.5189(2)
β (°)	104.023(2)	103.833(2)	103.672(2)	103.563(2)
***V* (Å^3)**	280.008(14)	274.139(13)	269.674(13)	266.912(14)
ρ (g/cm^3)	5.983	6.111	6.212	6.277
Collected reflns	1022	1948	1915	1821
R_{int}	0.059	0.070	0.071	0.067
Data/parameters	357/26	460/26	449 / 26	438 / 26
S	1.073	1.026	1.030	0.999
R1 (I>2σI)	0.0451	0.0433	0.0442	0.0418
***w*R2 (I>2σI)**	0.1016	0.0958	0.1079	0.0945

4.3 Results & Discussion:

4.3.1 Elastic Properties

An in depth discussion of the elastic properties for $GdPO_4$ was presented in Chapter 3. For convenience, Table 2, which gives elastic constants for volume and individual axes is reproduced here. As seen in Chapter 3, $GdPO_4$ is relatively incompressible with a unit cell volume decrease of only 4.68% over the 0−7.062(6) GPa pressure range, and has a bulk modulus (K_0) of 128.1(8) GPa (K′ = 5.8(2)). Consistent with the high bulk modulus for $GdPO_4$ the axial moduli (M_0) are also large, however the values of M_0 show a trend of decreasing axial compression in the order: [001] > [010] > [100]. This suggests that the chains of alternating polyhedra that lie parallel to [100] are more rigid than the directions perpendicular to them. This is consistent with the cross-linking of the chains through edge-sharing GdO_9 polyhedra resulting in flexibility in the [001] and [010] directions.

Table 4.2. Elastic Constants for $GdPO_4$. These values were derived from 3rd-order BM-EoS fits to the variable pressure unit cell parameters

			***a*-axis**	***b*-axis**	***c*-axis**
V_0 (Å^3)	280.017(18)	X_0 (Å)	6.33584(11)	6.84839(18)	6.6519(2)
K_0 (GPa)	128.1(8)	M_0 (GPa)	463(3)	389(3)	297(2)
K'	5.8(2)	M'	15.2(9)	15.8(11)	16.2(8)
K''(GPa^{-1})	−0.06991	M''(GPa)	−0.11929	−0.15689	−0.21983

4.3.2 Compression Mechanism

Due to the relatively high bulk modulus of $GdPO_4$ only small structural changes occur over the pressure range investigated. Indeed, the subtlety of the pressure-induced changes can be seen visually in Figure 4.2. This figure shows an overlay of the gadolinium coordination sphere at room-pressure and at 7.062(6) GPa, and it is immediately clear that there are no significant alterations in the structure between these two pressures. Therefore, to analyze how the structure changes, it is necessary to consider the effect of pressure on the larger features of the $GdPO_4$ structure rather than the small changes to individual angles/bonds, the magnitudes of which are within the estimated standard deviation for these parameters. To achieve this objective, we will consider the pressure-induced alterations to three components of the structure in turn: (i) the phosphate tetrahedra, (ii) the gadolinium polyhedra, and (iii) the inter-polyhedral distances.

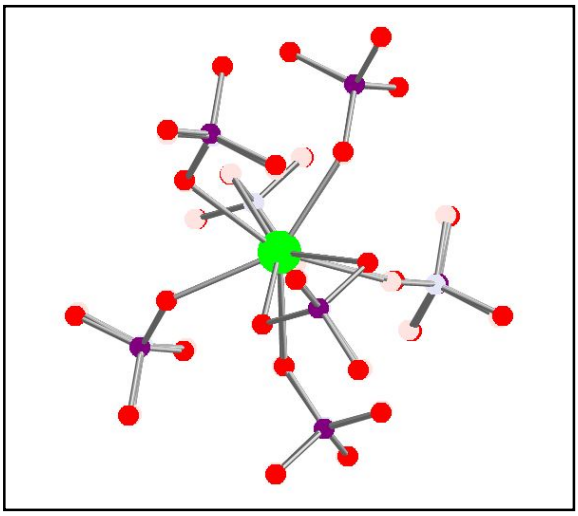

Figure 4.2: An Overlay of the Coordination Sphere of the Gd Cation at ~1 bar and 7.062(6) GPa. The room-pressure structure is shown in dark purple and red, while the 7.062(6) GPa structure is shown in light pink and blue.

To discern whether there are any changes to the phosphate tetrahedra in response to pressure, it is useful to first calculate distortion parameters for these polyhedra. The distortion parameters of interest are the elongation parameter ($<\lambda_{tet}>$) that quantifies the distortion to the tetrahedra due to variation in the bond lengths, and the bond angle variance ($\sigma_{(tet)}^2$) that quantifies the distortion due to variation in the bond angles within the tetrahedra.[6] For an ideal tetrahedron ($<\lambda_{tet}>$) = 1 and ($\sigma_{(tet)}^2$) = 0. Table 4.3 reports the values of these distortion parameters at various pressures. The PO_4 tetrahedra contain a fair amount of distortion. This is primarily due to deviations in the bond angles, as evident from the variance parameter that ranges from 22(3) to 29(4). The elongation parameter remains constant at 1.01, indicating that the bond lengths do not vary greatly within the tetrahedra. However, there is no statistically relevant change in either distortion parameter with increasing pressure. Therefore, the phosphate tetrahedra can be treated as rigid units when analyzing the overall compression mechanisms of $GdPO_4$ up to 7.062(6) GPa.

Table 4.3. Distortion Parameters for the Phosphate Tetrahedra at Select Pressures.

Pressure (GPa)	V_{tet} (Å^3)	l_0 (Å)	$<\lambda_{tet}>$	$(\sigma_{tet})^2$
~1 bar	1.826	1.527	1.01	29(4)
2.903(4)	1.816	1.524	1.01	23(3)
5.372(13)	1.807	1.521	1.01	29(3)
7.062(6)	1.820	1.525	1.01	26(3)

The gadolinium polyhedra were also analyzed for pressure-induced structural changes. The central gadolinium ion is coordinated to nine oxygen atoms with bond lengths ranging from 2.326(10) – 2.788(13) Å; eight of these nine bonds are ~2.45 Å while one bond is ~2.75 Å. The GdO_9 coordination geometry is similar to that of a heavily distorted mono-capped square antiprism (MCSAP, Fig. 4.3a). To date, no distortion parameters have been defined for a MCSAP polyhedron, so we will use the following parameters to quantify the distortion of the single symmetry independent GdO_9 MCSAP in $GdPO_4$: (i) plane centroid···centroid distance, pc···pc; (ii) the Gd ion offset, Δ(Gd···pc), where Δ(Gd···pc) = $a - b$ (Fig. 4.3a); (iii) the elongation parameter, $<\lambda_{sap}>$, which quantifies the distortion of the square antiprism due to variations in the M−O bond lengths (Eq. 1). This is equivalent to $<\lambda_{tet}>$ (*vide supra*); and (iv) the angular variance, $\sigma_{(mcsap)}^2$, which is equivalent to $\sigma_{(tet)}^2$, and is calculated with Equation 2:

$$< \lambda_{sap} >= \frac{1}{8}\sum_{i=1}^{4}\left(\frac{{}^{t}l_i}{{}^{t}l_0}\right)^2 + \frac{1}{8}\sum_{i=1}^{4}\left(\frac{{}^{b}l_i}{{}^{b}l_0}\right)^2$$

Equation 1.

$$\sigma_{(mcsap)}{}^2 = \frac{1}{11}\sum_{i=4}^{4}\left({}^{t}\theta_i - 90\right)^2 + \frac{1}{11}\sum_{i=4}^{4}\left({}^{b}\theta_i - 90\right)^2 + \frac{1}{11}\sum_{i=4}^{4}\left({}^{c}\theta_i - 90\right)^2$$

Equation 2.

where ${}^{t}l_i$ and ${}^{b}l_i$ are the measured lengths of the Gd−O bonds that define the sides of the top and bottom square pyramids, respectively. ${}^{t}l_o$ and ${}^{b}l_o$ are the ideal Gd−O distances for a perfect square pyramid with a volume equal to that of the top and bottom pyramid, respectively. Parameters ${}^{t}\theta_i$ and ${}^{b}\theta_i$ are the for O−pc−O angles within the bases of the top and bottom square pyramids, respectively; ${}^{c}\theta_i$ are the four O−pc−O angles between the oxygen atoms comprising the base of the top pyramid and the capping oxygen atom. These distortion parameters are shown in Table 4.4. For an ideal MCSAP, these parameters are $<\lambda_{sap}>$ = 1 and $\sigma_{(mcsap)}{}^2$ = 0. Under ambient pressure these parameters indicate that the MCSAP environment of the Gd^{3+} ion is heavily distorted, and this is primarily due to considerable deviation of the O−pc−O angles from 90° rather than a variation in the Gd−O bond lengths.

Table 4.4. Distortion Parameters for the Gadolinium Polyhedra at Select Pressures.

Pressure (GPa)	pc···pc (Å)	Δ(Gd···pc) (Å)	${}^{t}l_0$ / ${}^{b}l_0$ (Å)	$<\lambda_{sap}>$	$(\sigma_{mcsap})^2$
~ 1 bar	2.332(8)	0.669(10)	2.455/2.434	1.00	631(6)
2.903(4)	2.308(7)	0.688(9)	2.509/2.423	0.97	644(5)
5.372(13)	2.288(8)	0.708(7)	2.543/2.468	0.93	631(5)
7.062(6)	2.271(6)	0.722(9)	2.399/2.414	1.00	637(5)

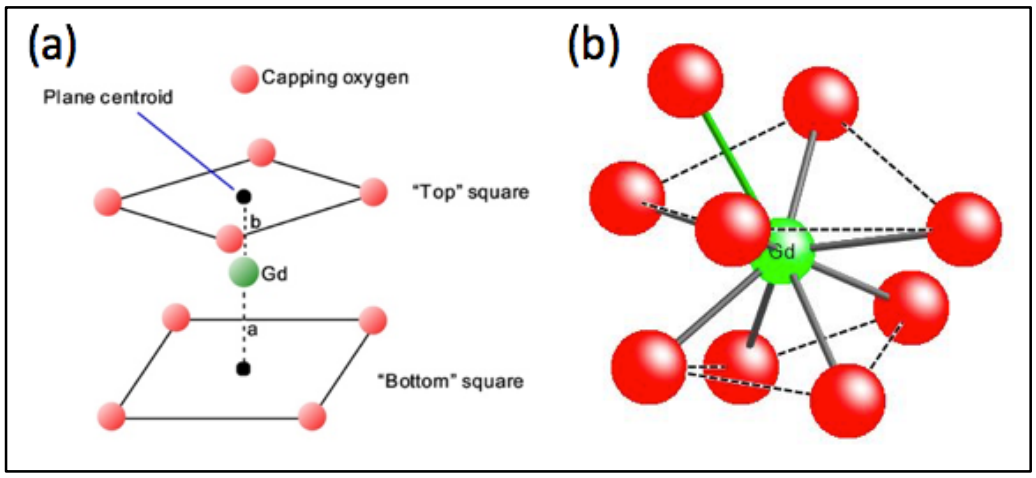

Figure 4.3: Representations of the Coordination Environment of the Gd Cations in $GdPO_4$. (a) Schematic representation of an ideal MCSAP; (b) Distorted MCSAP geometry of the Gd^{3+} ions in $GdPO_4$ under ambient pressure. The Gd−O bond involving the capping oxygen atom is shown in green.

There are no statistically relevant changes to the parameters $<\lambda_{sap}>$ and $\sigma_{(mcsap)}^2$ with pressure. However, there are statistically relevant changes to both the pc···pc distance and the Δ(Gd···pc) parameter with increasing pressure. As the pressure increases, the distance between the centroids of the square pyramid bases of the MCSAP decrease. Yet, the increase in the Δ(Gd···pc) parameter with pressure indicates that this is an asymmetrical compression (*i.e.* $\Delta a \neq \Delta b$). In fact, $\Delta b > \Delta a$ indicating that the Gd^{3+} ion is displaced towards the top plane of the MCSAP with increasing pressure. As shown in Figure 1, the Gd−O bond involving the capping oxygen atoms of the MCSAP polyhedra are orientated approximately parallel to the [100] direction. Therefore, these alterations to the MCSAP polyhedra can be envisaged as facilitating compression in this direction.

To evaluate the overall pressure-induced changes to the $GdPO_4$ structure it is beneficial to assess the secondary coordination sphere of the Gd^{3+} ions by considering the Gd···Gd distances between neighboring ions, as these can be determined reliably from our high-pressure XRD data (Table 4.5). Figure 4.4 is a pictorial representation of how these pressure-induced decreases in the Gd···Gd distances relate to the overall compression of the structure. The largest decrease occurs between $Gd\cdots^{edge}Gd^{i}$ and $Gd\cdots^{edge}Gd^{ii}$ (see Fig. 4.1b for atom labeling scheme) is 0.104 Å and these are aligned approximately parallel to the [100] and [010] directions. The two intermediate decreases of 0.058 Å (between $Gd\cdots^{edge}Gd^{iii}$ and $Gd\cdots^{edge}Gd^{vii}$) and 0.088 Å

(between Gd···^{edge}Gd^{xi}) are aligned closest to the [010] and [001] directions. Lastly, there is no statistical change in the Gd···Gd distance that would contribute to a reduction in the *c*-axis (Gd···^{edge}Gd^{xii}). This analysis indicates that the combination of these structural changes corresponds well with the measured elastic constants for $GdPO_4$ (Table 4.2) that shows a decrease in compression in the order: [001] > [010] > [100].

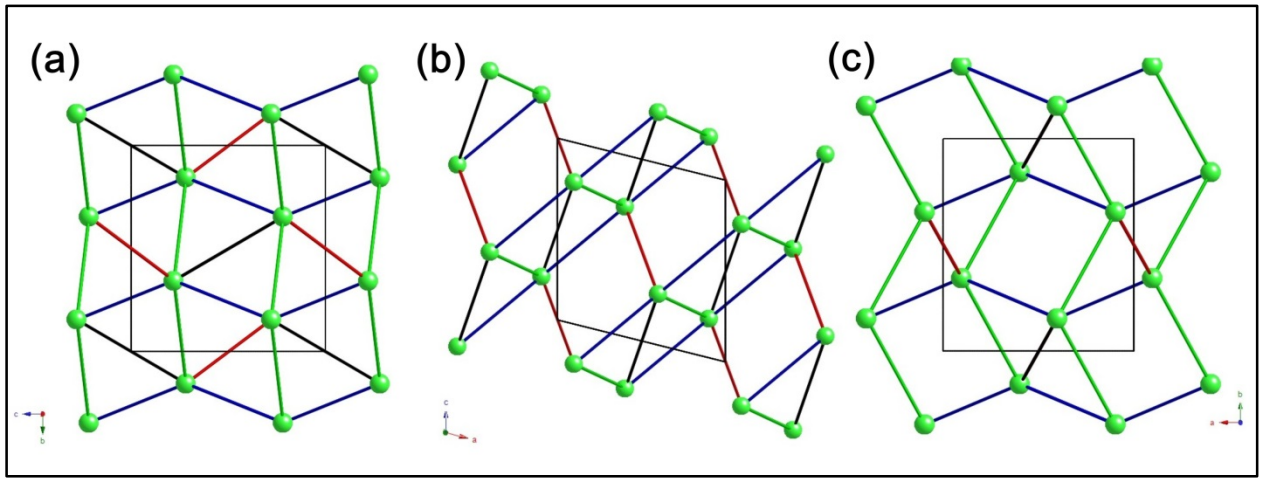

Figure 4.4: Pictorial Representation of Changes to the Distances Between Neighbouring Gd^{3+} ions. Green struts represent a 0.104(1) Å decrease, black a 0.088(3) Å decrease, blue a 0.058(1) Å decrease, and the red struts represent no change in these distances between ambient and 7.062(6) GPa: (a) view along [100]; (b) view along [010]; (c) view along [001]. The unit cell is shown in grey.

Table 4.5. Distances Between Gd Cation Positions at Select Pressures.

Distance	~1 bar	2.903(4)GPa	5.372(13) GPa	7.062(6) GPa	$\Delta(P_{min}/P_{max})$
Gd1···^{edge}Gd^{i}	4.0075(7)	3.9614(6)	3.9268(7)	3.9033(6)	0.104(1)
Gd1···^{edge}Gd^{ii}	4.0075(7)	3.9614(6)	3.9268(7)	3.9033(6)	0.104(1)
Gd1···^{edge}Gd^{iii}	4.2036(4)	4.1771(4)	4.1569(4)	4.1454(4)	0.058(1)
Gd1···^{edge}Gd^{vii}	4.2036(4)	4.1771(4)	4.1569(4)	4.1454(4)	0.058(1)
Gd1···^{edge}Gd^{xi}	4.2212(18)	4.1793(14)	4.1509(13)	4.1328(13)	0.088(3)
Gd1···^{edge}Gd^{xii}	4.0277(14)	4.0277(12)	4.0251(14)	4.0240(12)	0.00(4)

Symmetry codes: (i) -x+1/2,y+1/2,-z+3/2; (ii) -x+1/2,y-1/2,-z+3/2; (iii) x-1/2,-y+3/2,z-1/2; (vii) x+1/2,-y+3/2,z+1/2; (xi) -x,1-y,1-z; (xii) –x, 1-y, 2-z.

4.4 Conclusion

This chapter presented the structural compression mechanisms for a high-pressure study on $GdPO_4$. The results have shown that the compression mechanisms can explain the axial elastic constants for $GdPO_4$ where compression increases from: [100] < [010] < [001]. Analysis of high-pressure single-crystal diffraction data have established that the PO_4 tetrahedra act as rigid entities under pressure, and compression is enabled through adjustments to the O−Gd−P linkages that result in subtle alterations to the $GdPO_9$ polyhedra. These results importantly confirm the resilience of $GdPO_4$ to pressure as the first high pressure structural analysis completed on any of the rare-earth phosphate minerals.

References

[1] Boatner, L.A.; "*Structure and Properties of Monazite, Pretulite and Xenotime*" in: *Phosphates: Geochemical, Geobiological, and Materials Importance*, *Rev. in Mineralogy and Geochemistry*, Hughes, J. M.; Kohn, M.; Rakovan, J. (Eds.), Vol. 48, Mineralogical Society of America & the Geochemical Society, **2002**.

[2] Miletich, R.; Allan, D.R.; Kuh, W. F.; *High-Temperature and High-Pressure Crystal Chemistry*; Hazen, R. M., Downs, R. T. (Eds.); Mineralogical Society of America, Washington, DC, **2000**; Vol. *41,* 445–519.

[3] Angel, R. J.; Allen, D. R.; Miletich, R.; Finger, L. W. *J. Appl. Cryst.* **1997**, *30*, 461–466.

[4] Angel, R. J.; Bujak, M.; Zhao, J.; Diego Gatta, G.; Jacobsen, S. D. *J. Appl. Cryst.* **2007**, *40*, 26–32.

[5] Angel, R. J; Gonzalez-Platas, J. *J. Appl. Cryst.* **2013**, *46*, 252–254.

[6] Gibbs, G. V.; Ribbe, P. H.; Robinson, K. *Science* **1971**, *172*, 567−570.

Chapter 5: Conclusion

5.1 Concluding Remarks

The purpose of the research presented in this thesis was to better understand the influence of the REE cation on the spectroscopic, structural and thermodynamic properties of MPO_4 (M = trivalent lanthanide cation) compounds. This objective was achieved by multiple high pressure analyses of the structural and vibrational properties of $CePO_4$, $GdPO_4$ and $TbPO_4$, YPO_4, and $ScPO_4$. The cerium and gadolinium phosphates are isostructural with monazite ($P2_1/n$), whereas the remaining phosphates in this list are isostructural with xenotime ($I4_1/amd$). The study cumulated in a systematic assessment of the stability and elastic properties of these important phosphate minerals.

Raman spectroscopic data of $GdPO_4$ and $CePO_4$ monazite were compared with $ScPO_4$ and YPO_4 xenotime and all show excellent agreement with previous studies. Additional peaks not predicted by the factor group analyses are observed in the spectra of monazite and xenotime that may be due to infrared transitions activated by defects in the structures. All Raman peaks for the synthetic samples have symmetrical profiles and full widths at half maximum on the order of 10 cm^{-1}. In contrast the peaks of the natural specimen of $CePO_4$ (monazite) are much broader. This band broadening may be related to structural radiation damage or by the extensive incorporation of elements in the host structure.

The high-pressure Raman and diffraction analyses showed that no phase transitions occur for any of the minerals studied within the investigated pressure ranges (< 10 GPa). The high pressure Raman data show that the internal PO_4 stretching modes display the greatest shifts with pressure (moving to higher frequencies) while most of the lattice modes show little change with pressure. This indicates a changing environment around the PO_4 tetrahedra with pressure. Previous high pressure studies had indicated the possibility of pressure induced phase transitions (xenotime → anhydrite (possibly) → monazite → scheelite) occurring; however, no such structural alterations were observed in this study. Furthermore, the bulk moduli (K_0) for $GdPO_4$, $TbPO_4$, and $ScPO_4$ measured in this study are notably different from those previously reported in the literature. These disparities are believed to be a consequence of the variation in the experimental conditions under which measurements on these materials have been performed. Much of the currently available high pressure data for these materials have been collected under

conditions we expect to be non-hydrostatic, which results in the samples being subjected to unquantified shear stresses. Conversely, all high pressure experiments reported herein were conducted under hydrostatic conditions (no shear forces present). Comparison of these results has shown that both xenotime and monazite structures are sensitive to shear forces that alter both their elastic behavior, and can also induce phase transitions.

The bulk moduli determined in this study ($CePO_4$: 109(3) GPa; $GdPO_4$: 128.1(8) GPa; $TbPO_4$: 141(1) GPa; $ScPO_4$: 166(1) GPa) show an inverse linear relationship between the bulk moduli and the ionic radii of the REE cation in the MPO_4 structure. This trend supports the hypothesis that samples with the monazite structure, which contain the larger rare-earth cations, will be easier to compress than xenotime structures that incorporate smaller cations. Furthermore, this trend holds across the monazite and xenotime boundary, which implies that the structure topology has little to no effect on the bulk moduli of these minerals. A mathematical expression that quantify this relationship was determined from the bulk moduli measured in this study, and can be used to predict bulk moduli for all other rare-earth phosphates under hydrostatic conditions.

Comparison of the elastic constants for the natural $CePO_4$ [formula: $Ce_{0.44}La_{0.21}Nd_{0.18}Pr_{0.06}Gd_{0.04}Th_{0.03}Sm_{0.02}Ca_{0.01}Y_{0.01}(P_{0.98}Si_{0.02}O_4)$], sample measured in this study with those reported for a synthetic sample indicated no statistical difference between the two calculated K_0 values. In both cases both measurements were performed under similar experimental conditions. This finding also suggests that elastic constants determined for synthetic phosphate samples are similar to those for more chemically complex natural samples and can therefore be employed in geologic models.

As expected, the axial compressibilites (M_0) for the monazite and xenotime samples are related to arrangement the polyhedral chains within the structures. In monazite these lie parallel to the [100] direction, and in the xenotime structures they lie parallel to the [001] direction. For the monazite samples ($CePO_4$ and $GdPO_4$) the axial compressibilities increase in the order [100] < [010] < [001]. Whereas for the xenotime samples ($TbPO_4$, and $ScPO_4$) the order of increasing compressibility is [001] << [010]=[100]. In both structure types, the M_0 values suggest that compression is easier in the directions perpendicular to the polyhedral chains, and is hindered in the directions in which the chains are parallel. It is clear that the chains confer rigidity to the structures. It was also concluded that the compressibilities of the chains is

inversely proportional to the size of the lanthanide cation.

A single crystal high pressure diffraction study was completed for $GdPO_4$ (monazite) to elucidate the compression mechanisms operating in this compound. This study represents the first reported determination of the *structural* changes that occur in MPO_4 minerals in response to pressure. Due to the relatively high bulk modulus of $GdPO_4$, only small structural changes occurred over the investigated pressure range, 0−7.062(6) GPa. These small changes led to compression mechanisms being resolved from careful consideration of the pressure induced modifications to the polyhedra. The phosphate tetrahedra showed no structural changes and therefore can be regarded as rigid units. However, the Gd mono-capped square antiprism (MCSAP) polyhedra do show statistically relevant changes with pressure. This single structural study on $GdPO_4$, and the axial compressibility data for $CePO_4$, $TbPO_4$, $GdPO_4$, and $ScPO_4$ suggests that the compression mechanisms favored by MPO_4 compounds are primarily associated with alterations to the $REEO_x$ polyhedra. However, further experiments are necessary to confirm this hypothesis.

Kieffer models that were derived from the Raman data of $CePO_4$ and YPO_4 were developed and the heat capacities were calculated. The calculated heat capacities were within 1-3% of the reported experimental values. These models can therefore be extended to calculate additional thermodynamic properties such as enthalpy and entropy of these phosphate minerals at various pressures and temperatures and to determine the equilibrium phase boundary between monazite and xenotime. Preliminary calculations suggest that monazite and xenotime have the potential to be good geothermometers − minerals used to calculate the temperature history of geological formations. Further research is needed into the formation of this class of minerals with special attention on the effects of pressure.

In conclusion, the work presented in this thesis represents the first comprehensive study on a suite of MPO_4 (M = Tb, Gd, Ce, and Sc) minerals, which has allowed for direct comparison of their structural response to pressure. The results from this research have highlighted the potential of monazite/xenotime minerals as geothermometers, and have confirmed the value of continued investigations into their potential utility in the field of nuclear waste stewardship. Furthermore, it is hoped that our improved understanding of the thermodynamic and structural aspects of these technologically vital lanthanide ores will perhaps aid the development of improved extraction techniques and greater accuracy in locating new ore deposits – challenges

that will continue to confront current and future generations.

Looking towards the future there are a few directions in which to take this project. The first, in regards to the EoS study would be to conduct more hydrostatic high-pressure single-crystal studies on synthetic rare-earth phosphates. This would greatly add to the reliability of the trend seen in chapter three where there is an increase in bulk modulus with decreasing ionic radius of the rare-earth cation. It would also help discern if the trend is actually linear, or if it should be fit to a higher order equation. It would also elucidate whether this trend really holds across the monazite and xenotime boundary or if the two structures should be regarded separately. Another component to the EoS study, would be to subject these materials to non-hydrostatic conditions to see if the shear stresses and their affect can be quantified. If a phase transition is seen under these known non-hydrostatic conditions, it could help map the uncertainty of what structures take part in the transition and how the shift from one structure to another occurs at the atomic level. Lastly another study that would be interesting would be to do high pressure work on other ABO_4 structures that had REEs but different elements substituting for phosphorous such as sulfur, arsenic and chromium. This would show how changing the "B" cation affects expected trends on the Bastide diagram and show what effect the phosphorus has the bulk moduli compared to the REE.